Chapter 4

Relativistic jets from Collapsars.

An astrophysical phenomenon which also involves flows with velocities very close to the speed of light are gamma-ray bursts (GRB). This is the reason why hydrodynamic models (including, in some cases, the appropriate micro-physics) have become a main research tool in order to understand the GRB phenomenon (*e.g.,* Piran, Shemi & Narayan 1993; Mészáros, Laguna & Rees 1993; MacFadyen & Woosley 1999; Ruffert & Janka 1998, 1999a, 1999b; Aloy *et al.* 1999c).

We are going to present the observational framework in which GRBs are included (Sect. 4.1). The standard model trying to explain the current observations will be summarized in Sect. (4.1.1). The next subsection (4.2) gives an historical overview of the numerical simulations in this field. The modifications that we have included in the code GENESIS to treat a background Schwarzschild metric are discussed in Sect. 4.3.2, and the EOS employed in our calculations is described in Sect. 4.3.3. Section 4.3 deals with the relativistic version of the collapsar model introduced, in the Newtonian case, by MacFadyen & Woosley (1999) (MW99 in what follows).

4.1. Phenomenology

Gamma-ray bursts are known observationally since over 30 years. They were discovered by chance by American military satellites of the VELA class, which were developed at Los Alamos in order to detect clandestine nuclear tests in space by their associated gamma-ray emission. The detected radiation consisted of gamma-ray flashes lasting a few seconds. The results of these detections where published five years afterwards (Klebesadal, Strong & Olsen 1973). This paper reported 16 short bursts of photons in the energy range $0.2 - 1.5\,\mathrm{MeV}$ lasting between $0.1 - 30\,\mathrm{s}$ and having a complex time-structure (mainly in the longer bursts).

The phenomenology of these first set of bursts has proven to be the common one of GRBs. These common features, that define a GRB, are described in the following sections (for a longer review see, *e.g.,* Piran 1999 –PI99– or Daigne 1999).

Temporal properties. GRBs are very short events, with a typical duration between several milliseconds and several hundreds of seconds, showing a large variability even at the millisecond scale (suggesting an association between GRB sources with very compact progenitors). They show a bimodal time-distribution, the border between the two groups being at ~ 2 s. The first group is composed of *short* bursts centered around $0.1\,\mathrm{s}$, while the second group consists of *long* bursts (more numerous) centered at about $15\,\mathrm{s}$. The time-structure is very different from burst to burst. There are GRBs which show a simple and regular structure, whereas others have a very complex profile (Norris *et al.* 1996, explain the complex structure as the superposition of several pulses). From the data collected by the BATSE[1] experiment (Kouveliotou *et al.* 1993) and PHEBUS (Dezalay *et al.* 1996) mission it seems that short GRBs are harder than the long ones. Additionally, it is more difficult to detect short bursts, and there exist indications that short GRBs are closer than the longer ones, and that they form a separate subgroup (Mao, Narayan & Piran 1994).

Spectral properties. GRB spectra are non-thermal. The observed energy flux as a function of the energy ($E^2 n(E)$ or νF_ν; where E, $n(E)$, ν and F_ν are the energy, the number of counts per unit of time, area and energy, the frequency and the flux per frequency, respectively) can be well described by one or a combination of several power laws. The maximum of the energy distribution corresponds to an energy, E_p (the energy peak), which is characteristic of each GRB and usually is

[1]BATSE (*Burst and Transient Source Experiment*) is an experiment launched in 1990 on board of the satellite CGRO (*Compton Gamma-Ray Observatory*).

about several hundreds of keV. The spectra can be fitted by the following function (Band *et al.* 1993):

$$n(E) = A\left(\frac{E}{100\mathrm{keV}}\right)^{\alpha}\exp\left(-\frac{E}{E_0}\right) \quad \text{for } E \leq \frac{E}{\alpha-\beta}$$
$$n(E) = A\left(\frac{(\alpha-\beta)E_0}{100\mathrm{keV}}\right)^{\alpha}\exp(\beta-\alpha)\left(\frac{E}{100\mathrm{keV}}\right)^{\beta} \quad \text{for } E \geq \frac{E}{\alpha-\beta}$$

where α and β are the slopes of the power laws at low and high energy, and $E_0 = E_p/(2+\alpha)$. The values of α and β lie in the range $\alpha \in [-3/2, -2/3]$ and $\beta \in [-3, -2]$.

The observed fluence on earth is $10^{-5} - 10^{-7}$ erg/cm^2 the upper limit depending on the duration of the observation, and the lower limit depending on the detector. Redshift measurements of half a dozen of GRBs indicate that, for isotropic emission, the total energy is of the order of $10^{51} - 10^{54}$ erg (PI99). Recent observations (*e.g.*, GRB 990510, Harrison *et al.* 1999) suggest that the radiation is beamed (Sari, Piran & Halpern 1999; Rhoads 1999), reducing this energy by two orders of magnitude.

Spatial distribution. The BATSE experiment has observed more than 2000 events since 1991 (at a rate of $\sim$ 1 per day) in its systematic all-sky coverage. The positional accuracy of this detector is quite low the typical error-boxes being $\sim 1-2$ degrees for the brightest bursts, and more than 5 degrees for the fainter ones. However, there are some bursts whose locations have been pinned down with a precision of minutes of arc or better by triangulation experiments involving deep space probes (*e.g.*, the ULYSSES spacecraft). The technique utilizes the rapid time structure which, when recorded and timed by detectors separated by 10 light-minutes or more, allows for an accurate positioning. The statistical analysis of the BATSE data shows that the bursts are isotropically distributed (BATSE restricts any dipole or quadrupole anisotropy below the few per cent level and shows no evidence for clumping on smaller scales), but not homogeneously (see *e.g.*, Rees 1997). This heterogeneity is found in $\log N - \log P$ diagrams, where $N(P)$ is the number of bursts which have an intensity at maximum larger than a threshold P. These number-versus-intensity diagrams of the events tell us whether they are uniformly distributed in Euclidean space or not. The reason is that if the events were uniformly distributed, one would expect the number of bursts should be proportional to the volume observed, *i.e.*, $N \sim R^3$. As the luminosity drops with distance as $P \sim R^{-2}$, one should find that $N \sim P^{-3/2}$. Consistently, a homogeneously distributed sample of bursts in Euclidean space must have a slope equal to $-3/2$ in the $\log N - \log P$ plane. The GRB observations are in agreement with such a distribution in the case of short (*i.e.,* powerful) bursts (Katz & Canel 1996; Tavani 1998), but their distribution significantly deviates from this slope for longer (*i.e.,* fainter) bursts (*i.e.,* small values of P).

Interpretation. A key point for the interpretation of the results is the distance at which the bursts occur, because this strongly influences (1) the estimated energetics of the GRB events, (2) the homogeneity of their distribution, and (3) their *production rate*. Concerning the energetics, three different characteristic GRB energies can be derived depending on their distance. Assuming that the energy of each burst is isotropically released these energies are 10^{37} erg, 10^{41} erg, or 10^{51} erg for bursts occurring in the Galactic Disc (at distances of a few hundred of pc), in the Galactic halo (at distances of tens kpc), or at cosmological distances, respectively.

For years a controversial debate has been taken place whether GRBs are local or cosmological (see *e.g.,* Fishman & Meegan 1995; Mèzáros 1995; Piran 1997). However, a galactic origin has to be rejected, because the meanwhile extensive BATSE catalog shows an isotropic distribution of GRBs over the sky, and no source enhancement either towards the plane of the galaxy or towards the galactic center. Moreover, the recent redshift determinations (the first one obtained was $z = 0.695$ for GRB 970228; van Paradijs *et al.* 1997) prove the cosmological origin at least of the majority of GRBs. Observed redshift values are in the range $0.7 \leq z \leq 3.4$ implying emitted gamma-ray energies of $2 \times 10^{51} \leq E \leq 2.3 \times 10^{54}$ erg for an isotropically radiating source. The cosmological origin of the GRBs is consistent with the distribution of bursts in the $\log N - \log P$ plane. Actually, the deviation from the $-3/2$ slope can be interpreted as a consequence of the expansion of the Universe (which is, in addition, consistent with the redshift measurements). In fact, the point at which the deviation from the slope $-3/2$ is observed gives one information about the characteristics and distribution of the GRBs (see *e.g.,* Daigne 1999).

Nonetheless, this picture was challenged by the detection of the Type Ib/c supernova SN 1998bw (Galama *et al.* 1998) within the error box of GRB 980425 (Soffitta *et al.* 1998; Pian *et al.* 1999) whose explosion time is consistent with that of the GRB. BeppoSAX detected two fading X–ray sources within the error box, one being positionally consistent with SN 1998bw (Pian *et al.* 1999)[2].This suggests a relationship between GRBs and SNe Ib/c, *i.e.*, core collapse supernovae of massive stellar progenitors which have lost their hydrogen and helium envelopes (Galama *et al.* 1998; Iwamoto *et al.* 1998; Woosley, Eastman & Schmidt 1998). As the host galaxy of SN 1998bw has a redshift of $z = 0.0085$ (Tinney, Stathakis & Cannon 1998), this has led Castro-Tirado (1999) to estimate the isotropic gamma-ray energy emission of GRB 980425 to be $E_\gamma = 7 \times 10^{47}$ erg (*i.e.*, more than four orders of magnitude fainter than a typical cosmological GRB).

Depending on whether the number of bursts is correlated or not with the stellar formation rate, one can argue:

a) If there is no correlation, the expected redshift for the burst distribution should be $z \sim 1$, the typical energy of an event in gamma-rays should be $E_\gamma \sim 10^{51}(\Omega/4\pi)$ erg (Ω is the solid angle into which the emitted radiation may be beamed), and considering the observed frequency, the burst production rate should be $\sim 10^{-6}(4\pi/\Omega)$ GRB/year/galaxy.

b) If there is a correlation, the effect of the expansion of the Universe would be delayed, and the typical redshift might be $z \gtrsim 3$. The energy per event would be larger than in the previous case, and the production rate smaller ($\sim 10^{-7}(4\pi/\Omega)$ GRB/year/galaxy).

Afterglow observations. The BATSE instrument does not allow for an accurate positioning of the GRB sources and, therefore, it has been very difficult to identify optical counterparts within the instruments error box. Leaving aside the large number of possible candidates for a given burst detection, one of the main problems of this search is that the optical detection starts some time after the burst has been observed by the gamma-ray satellites and, consequently, possible observations in other wavelengths (X-rays, optical or radio bands) are delayed with respect to the burst itself. Thus, what is actually observed is the “afterglow” of the emission.

[2]However, there exist a debate about the truthfulness of this association, see *e.g.*, Wang & Wheeler 1998, Kippen *et al.* 1998.

The Italian Dutch satellite, BeppoSAX, discovered the first X-ray afterglow for GRB 970228 (Costa *et al.* 1997). Since then, more than two dozen X-ray afterglows have been detected. If an X-ray detection happens, the size of the error box is reduced to 50 arcseconds to 3 arcminutes. With this more accurate position, it is possible to start to look for optical counterparts (using ground based telescopes) with a delay smaller than one hour. However, as BeppoSAX can trigger only long bursts, it is not known whether short bursts also have afterglows. If the optical counterpart is seen, the localization of the object is obtained within an error box of ~ 1 arcsecond size. Moreover, if a radio detection is also successful, the positioning is enhanced up to ~ 1 milliarcseconds. Optical (*e.g.,* van Paradijs 1997) and radio (*e.g.,* Frail *et al.* 1997) afterglows have been discovered in about half of the cases in which X-ray afterglows have been seen. A remarkable feature of the VLBI detection of GRB 970508 has been the observation of a superluminal motion of the emission region (Frail *et al.* 1997) indicating that relativistic expansion of the matter is responsible for the emission.

The main observational properties of the afterglow emission are (PI99):

- The energetics of the process can be estimated from the late phases of the optical afterglows (Galama *et al.* 1998; Granot, Piran & Sari 1999; Wijers & Galama 1998; Vreeswijk *et al.* 1999). The overall energy emitted in the afterglow ($10^{50} - 10^{52}$erg) is a fraction of the one emitted during the GRB. The characteristic energy of the emission decays from the X-ray band to the radio band. Such behavior can be interpreted as the emission of an ultrarelativistic wind braked by its interaction with the ambient medium (Daigne 1999; Daigne & Mochkovitch 1999).

- The afterglow light curves decay in most cases following a single power law in time: $F_\nu = t^{-a}$, with $a \sim 1.2$. Nevertheless, $a \sim 2$ fits much better the bursts GRB 980326 (Grot *et al.* 1998) and GRB 980519 (Halpern *et al.* 1999). In other two cases, GRB 990123 (Kulkarni *et al.* 1999a) and GRB 990510 (PI99) that power-law is broken in two parts ($a \sim 1.1 - 1.2$ to $a \sim 2$), leading to the interpretation of beaming in the GRB emission (Sari, Piran & Halpern 1999). Obviously, such a beaming could reduce the energy release of the GRB by one or two orders of magnitude.

- The GRB 990123 has shown, for first time, a prompt optical emission, *i.e.,* the optical detection was done at the same time than the burst itself, using the ROTSE experiment (Akerlof *et al.* 1999); therefore, this emission is not exactly an *afterglow*, but shows the whole history of the GRB in the optical spectrum. The emission is peaked with a 9th magnitude signal which lagged 70 s after the gamma-ray peak and coincided with the prompt X-ray peak.

4.1.1. The standard model: the relativistic fireball

The observed gamma-rays reveal that GRB spectra are non-thermal. This indicates that the observed emission emerges from an optically thin region. However, the fast variability of the source ($\delta t \leq 1$ s) implies that the emission region is very compact ($\sim c\delta t$). Moreover, gamma-ray energies sometimes exceed 1 MeV, *i.e.,* they are above the pair production threshold in the rest frame. These facts along with the estimate of the number of photons with energies above 500 keV shows that the source should be quite optically thick to pair creation (*e.g.,* Fenimore, Epstein & Ho 1993) and, therefore, the source cannot emit non-thermally. Theoretically, this *compactness problem* has been overcome assuming that the emission region is moving ultrarelativistically towards us (Ruderman 1975; Goodman 1986; Krolik & Pier 1991). This is the basis of the *fireball model*, in which slowing relativistic ejecta produce the GRB and its afterglow. The observed gamma-rays are produced by the synchrotron or synchrotron self-Compton emission of the relativistic electrons that have been efficiently accelerated by shocks.[3] Such shocks can be either internal, *i.e.,* within the plasma (Narayan, Paczyński & Piran 1992; Paczyński & Xu 1994; Rees & Mészáros 1994) or external, *i.e.,* due to the interaction with the ambient medium (Mészáros & Rees 1992).

External shocks are collisionless and become effective at $\min(R_{W_s}, R_\Delta)$, where $R_{W_s} \equiv l/W_{s0}^{2/3}$ and $R_\Delta \equiv l^{3/4}\Delta^{1/4}$ (Sari & Piran 1995). W_s and Δ are the Lorentz factor and the width of the shell (in the observer frame), and W_{s_0} is the initial value of the shell Lorentz factor. The radius within which the rest mass energy of the

[3] Note the parallelism between this emission mechanism and the one which works in extragalactic jets (see §3.3).

external material, whose density is n_{ism}, equals the initial energy of the ejecta, E_0, is known as the Sedov length, $l \equiv (E_0/[(4\pi/3)n_{ism}m_pc^2])^{1/3}$. Some typical values of the previous quantities are: $l \sim 10^{18}$cm and $R_{W_s} \sim R_\Delta \sim 10^{15} - 10^{16}$cm. However, external shocks may not to be the only cause for the GRB emission, because (1) they cannot produce efficiently the highly variable temporal structure seen in GRBs (Sari & Piran 1997; Fenimore, Madras & Nayakshin 1996), because (2) the lack of any correlation between the width of late sub-pulses (produced when the Lorentz factor is lower and at larger radii, so that they should be longer) and the time of arrival (Fenimore, Ramirez & Summer 1998), and because (3) the invoked mechanism to account for the variability of GRBs in this case (inhomogeneities in the external media –Dermer & Mitman 1999–) is extremely inefficient (Sari & Piran 1997).

The other possibility to explain the emission of GRBs are internal shocks. The non-linear hydrodynamic evolution of the plasma may lead to the growth of internal shocks. It is assumed that faster shells overtake slower ones and collide, converting some of their kinetic energy into internal energy. According to PI99, internal shocks would take place at $R_{int} \sim \delta W_0^2$, where δ is a typical length scale of the problem. Actually, $\delta = c\delta t$ can be inferred from the observed temporal variability $\delta t \leq 1\,\mathrm{s}$ indicating that $R_{int} \sim 10^{13}$cm. If the shocks are formed earlier the radiation does not escape (the fireball is optically thick). The observed GRB time scales reflect the time scales of the "inner engine" (Kobayashi, Piran & Sari 1997), and their duration corresponds to the time of activity of the central engine. Another evidence for the internal shock model is the lack of a direct scaling between the GRB and the afterglow. Nonetheless, internal shocks can extract only a fraction of the total energy (Mochkovitch, Maitia & Marques 1995; Kobayashi, Piran & Sari 1997; Daigne & Mochkovitch 1998). The remaining energy would be extracted later via external shocks giving rise to additional emission at different wavelengths (Sari & Piran 1997).

Let us note that a relativistic expansion reduces the necessary energy budget of the photons because of the relationship between the frequencies in the observers frame (ν) and in the proper frame of the matter moving relativistically (ν'): $\nu = \mathcal{D}\nu'$ (Rybicki & Lightman 1979), where $\mathcal{D}$ is the Doppler factor (defined in Ap. D). In addition, BATSE observations put a constraint on the value of the mean Lorentz factor in the expanding fireball, because they show no indication of high-energy photon-photon collisions (which would enhance the opacity via annihilations $\gamma+\gamma \rightarrow e^{+}+e^{-}$). This means that the interaction cross sections of the photons are pretty small, or would strongly depend on the Lorentz factor. Actually, as matter is moving relativistically with a Lorentz factor W, the emission (*i.e.*, the photons' trajectories) is beamed in a rest frame within a solid angle of $\sim 1/W$. Larger Lorentz factors give more beaming, and the trajectories of the photons tend to become parallel in the ultrarelativistic limit. Hence, the probability of interaction decreases, because the momentum of the photons is directed mainly in radial direction (the opacity due to electrons and pairs is reduced by a factor $\sim W^{4}$, *e.g.*, Rees 1997). In order to overcome the problem of the photon-photon interactions many authors have arrived to a consensus on the minimum value of the mean Lorentz factor required for the fireball of $W \geq 100$ (*e.g.*, Baring 1995). Such a high Lorentz factor can only be attained if the baryon loading is sufficiently small. If one releases an energy E into a mass M (*initially*), a measure of the baryon loading is the ratio $\frac{1}{\eta} = Mc^{2}/E$. Assuming that all the energy is converted into kinetic energy, the final Lorentz factor will be $W = E/Mc^{2} = \eta$. Thus, a baryon loading $\leq 10^{-2}$ is required in order to obtain $W \geq 100$.

4.1.2. Models for the central engine

The astrophysical scenarios in which the GRBs are produced are still unknown. The main reason is the lack of observations which are detailed enough to resolve the host galaxy or the "burster engine". As GRBs are most probably born at cosmological distances, I will only give a brief review of the theoretical models that consider such cosmological scenarios (the reader interested in a more extensive overview is addressed to the reviews by Blaes 1994, Fishman & Meegan 1995 or Hartmann 1996).

The cosmological origin of GRBs was first proposed by Prilutskii & Usov (1975) and Paczyński (1986). In these early models, bursts were thought to originate in classical extragalactic sources (galaxies, quasars) or in other more exotic objects, like super-conducting cosmic strings or through a random pattern of gravitational radiation which is focused by a distant and steady source. More modern theories involve the coalescence and merging of neutron star binary systems, or the accretion onto a BH in a "failed" supernova.

If GRBs are cosmological, the typical energy of a burst should be $\sim 10^{51} - 10^{54}$ erg. Moreover, the temporal profiles of these events show a fast variability indicating that the size of the GRB's progenitors should not be larger than a few light-milliseconds. Thus, promising astrophysical sources of GRBs involve one or more compact objects of stellar size (*i.e.,* with a mass of a few solar masses). In principle, such compact objects can provide the required energy (after all, whenever a supernova goes off, the binding energy of a neutron star is released in a fraction of a second, and this amounts to 10^{53} erg).

In order to explain the amount of energy released in a GRB ($\sim 10^{51} - 10^{54}$ erg), the necessary Lorentz factors ($\sim 10^2 - 10^3$), the observed rapid variability of the emission (to occur at radii in the range $\sim 10^{14} - 10^{16}$ cm) and the necessary low baryon loading ($\sim 10^{-3} - 10^{-5}$ or $\lesssim 10^{-6} M_\odot$), various catastrophic collapse events have been proposed. These can be categorized as follows:

1) Coalescence of compact binary systems. This group includes NS/NS mergers (Pacyński 1986; Goodman 1986; Eichler *et al.* 1989; Narayan, Pacyński & Piran 1992) and NS/BH mergers (Narayan, Pacyński & Piran 1992; Mochkovitch *et al.* 1993). Recently, the coalescence of a NS or BH with a white dwarf (Fryer *et al.* 1999) or with the Helium core of a red giant has been proposed, too (Fryer & Woosley 1998). A binary NS/NS system, that may survive for $\sim 10^9$ years, will eventually coalesce when gravitational radiation drives both objects together. The final merger, leading probably to the production of a Kerr BH, happens in a fraction of second, and the energy released during the merging process is $\sim 10^{54}$ erg. It is also possible that a $\sim 0.1\, M_\odot$ accretion disk forms around the BH and is accreted within a few seconds, then producing internal shocks leading to the GRB (Katz 1997). The calculated event rates for such phenomena are 100 per year at a distance smaller than 200 Mpc (Fryer *et al.* 1999). This rate is a tenfold larger if one considers NS/BH mergers. Both rates are compatible (if the beaming factor $\Omega/4\pi$ is not very small and almost every merger produces a GRB) with the hypothesis that the GRBs are not correlated with the stellar formation rate (see previous subsection), in which

case a burst frequency of $\sim 10^{-6}(4\pi/\Omega)$ GRB/year/galaxy is expected.

2) *Hyper-accretion* onto compact objects resulting from the gravitational collapse of massive stellar cores. This category includes two families of models: the *hypernovae* (Pacyński 1998) and the *collapsars* (Woosley 1993). The hypernova model assumes that a core of a massive rapidly spinning star collapses directly to a BH without producing a supernova. A collapsar is the result of a failed Type Ib/c supernova which is produced by the gravitational non-spherical collapse of the rotating iron core of a Wolf-Rayet star. The likely result of both models is the formation of a Kerr BH with a $0.1 - 1\ M_{\odot}$ dense viscous torus around it. The matter is accreted at a very high rate ($\sim 1\,\mathrm{M_{\odot} s^{-1}}$; Popham, Woosley & Fryer 1998). Both scenarios are quite similar but they differ in the energy extraction mechanism: while a hypernova releases $\sim 10^{54}\,\mathrm{erg\,s^{-1}}$ of kinetic energy by tapping the rotational energy of the Kerr BH using the Blandford & Znajek (1977) mechanism, a collapsar converts the gravitational binding energy released by accretion into neutrino and anti-neutrino pairs (via viscous dissipation of energy in the accretion torus), which in turn annihilate into electron-positron pairs. It is hard to determine the minimum mass required for a progenitor star to produce any of these collapses but most probably it should be a main sequence star of several dozens of solar masses (which are necessary in order to produce, by evolution, a stellar core of $10 - 15 M_{\odot}$). In any case, a "fireball", which will also contain the baryons present in the neighbourhood of the BH, will be produced reaching a luminosity ~ 300 times larger than that of a normal SN. For the collapsar model, provided the baryon load of the fireball is not too large, the baryons are accelerated together with the $e^+ e^-$ pairs to ultrarelativistic speeds with Lorentz factors $> 10^2$ (Cavallo & Rees 1978; Piran, Shemi & Narayan 1993). The bulk kinetic energy of the fireball then is thought to be converted into gamma-rays via cyclotron radiation and/or inverse Compton processes (see, e.g., Mészáros 1995). The event rate for these models ($\sim 10^{-3}$ per year and galaxy) is larger than that of the coalescing binary systems. However, strong effects due to stellar evolution are expected (a typical $30 M_{\odot}$ star that forms a Wolf-Rayet and then collapses lives for 10^6 years only). As the event rate is correlated with the star formation rate (see 4.1) the number of events expected is $< (4\pi/\Omega)10^{-7}$ per year and galaxy. Consequently, to be consistent with this rate, the beaming should be quite large, or only a fraction of core collapses do produce GRBs.

The two main differences between both families of models are their locations and environment. A typical binary system formed by two NS needs $\sim 10^9$ years to merge. During this time the system can travel tens of kpc due to the large kick velocity acquired during the two supernovae explosions (Tutukov & Yungelson 1994). A massive star on the other side only lives for a few million years and hence cannot move far during its lifetime, *i.e.,* it explodes within the star forming region where it was born. The environment around a Wolf-Rayet star is more complex and dense than that around a binary system because the star has lost an important part of its mass due to the ejection of the outer shells. However, current observations have been unable to give any insight on this issue (the position of the bursts in the host galaxies has not been accurately established yet), although some authors claim that GRBs are produced in star formation regions (Fruchter *et al.* 1999) and possibly, the optical afterglow might be heavily obscured by dust commonly present in such regions (Jenkins 1997). In MW99 is said that the hypernova/collapsar model can explain better long and very energetic bursts than the coalescence of binary systems. The reason being that the dynamical time to accrete the matter of the torus formed due to the merger of the two NS is very small (depending on the viscosity of the model –which is still uncertain– it can be, at most, 0.5 s), and according the standard model, the duration of a burst depends on the life-time of the engine.

All the models just discussed can be subdivided into two groups according to the energy extraction mechanism, namely those which invoke hydromagnetic energy extraction, and others that rely on the dissipation of energy in the accretion disk via neutrino emission. Within the first group of models one considers two different possibilities: (1) extremely intense magnetic fields ($\sim 10^{15} - 10^{16}$ G) extract matter and energy from the disk and the BH itself via the Blandford-Znajek mechanism (Usov 1994; Mészáros & Rees 1997), or (2) reconnection of the magnetic field lines in the corona of the disk (which is much less dense than the disk) liberates enough thermal energy to power a relativistic wind (Narayan, Paczyński, & Piran 1992). The second group of models was proposed by Mészáros & Rees (1992) and Mochkovitch *et al.* (1993), (1995). In this case neutrinos preferentially deposit their energy in a region near the rotation axis, because the inner boundary of the accretion torus is almost parallel to the axis thus favoring "head-on" collisions of the neutrinos.

4.1.3. An afterglow model

The afterglow is the emission that follows a GRB at frequencies gradually declining from X-rays to visible and radio wavelengths. Soon after the first BeppoSAX observations it was suggested by Paczyński & Rhoads (1993) (for the radio afterglow) and independently by Katz (1994) (for the optical afterglow) that the long term interaction of the relativistic ejecta with the external medium will produce a low frequency afterglow. Mészáros & Rees (1997) and Vietri (1997) pointed out that afterglows are produced by the external blast wave moving ahead of the fireball (sweeping the interstellar matter). This afterglow is the long time continuation of the GRB and should have properties similar to the GRB itself, if the emission of the GRB is produced by external shocks. However, as we have noted above, the external shock model for GRBs has several problems. This leads one to the assumption that GRBs themselves emit due to the presence of internal shocks. In the currently accepted "Internal-External" model the GRB and the afterglow are produced by two different processes, i.e. no direct scaling between both is expected.

The radio afterglow of GRB 970508 has provided a direct confirmation of the fireball model, because it has shown an evident flickering (decreasing with time) for about a month. The transition from the flickering to the non-flickering regime has allowed Frail *et al.* (1997), using the theoretical analysis of Goodman (1997) for the determination of angular sizes from *refractive radio scintillation*, to estimate that the afterglow had a size of $\sim 10^{17}$cm one month after the burst. Katz & Piran (1997) estimated a similar size independly, suggesting that the source could become optically thick, if the synchrotron self-absorption rises the spectrum in radio frequencies. Using the observed flux and an estimate of the temperature of the emitting regions they were able to obtain the size of the emitting region. Both observations provide evidence (for first time) that the fireball is expanding relativistically.

4.1.3.1. Emission properties

The generic emission process for both the GRB and the afterglow is synchrotron. The energy distribution of the emitting electrons has the same power law distribution than in the case of relativistic jets (Eq. D4), but the spectral index of the distribution that fits better the observations is $p \sim 2.5$. For this value of p the distribution diverges at low energies. Thus, like for extragalactic jets, this produces a low energy cutoff (Eq. D6).

The emission that originates the afterglow comes from the external shock surrounding the fireball. Actually, such a shock has a more complex structure that fits better with that of a blast wave. The properties of this blast wave can be derived from the synchrotron spectrum (Pacholczyk 1970) of a population of electrons with the addition of self absorption at low frequencies and cooling break, according to Sari, Piran & Narayan (1998). The spectrum depends on four parameters:

- The synchrotron frequency, ν_m, which corresponds to $W_{e,min}$ (or E_{min}; see Eq. D6).

- The cooling frequency, ν_c. This is the synchrotron frequency of an electron that cools during the local hydrodynamic time scale: $E_c/P_{\nu_c}(E_c) = t_{hyd}$ (P_{ν_c} is the power emitted by a single electron due to synchrotron radiation; E_c is the energy corresponding to ν_c). Fast cooling (*i.e.*, typical electrons are cooled within times smaller than t_{hyd}) implies that high energy electrons will cool rapidly for $\nu_c < \nu_m$. Slow cooling leads to a reduced cooling of low energy electrons for $\nu_m < \nu_c$.

- The self-absorption synchrotron frequency, ν_{sa}. The same electrons that produce the synchrotron radiation can also scatter with low energy photons via inverse Compton. Self-absorption may appear at late time typically in radio emission (*e.g.*, Paczyński & Rhoads 1993). It is defined (*e.g.*, Rybicki & Lightman 1979) as the frequency for which the optical depth along the line of sight is equal to one ($\tau(\nu_{sa}) = 1$).

- The maximum flux $F_{\nu,max}$.

The combination of all these effects (fast or slow cooling, presence or not presence of self-absorption) leads to a spectrum which is a combination of four power laws, where three of the four slopes are fixed and one is depending on whether or not the electrons are rapidly cooled. The corresponding flux can be written (at a fixed time) as $F_\nu \propto \nu^\beta$ with:

$$\beta = \begin{cases} 2 & \text{for } \nu < \nu_{sa} \text{ - self absorption;} \\ 1/3 & \text{for } \nu_{sa} < \nu < \min(\nu_m, \nu_c); \\ -1/2 & \text{for } \nu_c < \nu < \nu_m \text{ - fast cooling;} \\ -(p-1)/2 & \text{for } \nu_m < \nu < \nu_c \text{ - slow cooling;} \\ -p/2 & \text{for } \max(\nu_m, \nu_c) < \nu. \end{cases} \tag{4.1}$$

This instantaneous spectrum is valid for the GRB and the afterglow phases. However, as the GRB stage involves simultaneous emission from multiple shocks, the resulting spectrum may be more complicated PI99. To determine the light curve one needs ν_{sa}, ν_m, ν_c, and $F(\nu_m)$ as a function of time (all other fluxes are determined by these quantities). Moreover, for comparison with the observations it is necessary to express the instantaneous size of the fireball (R) and its Lorentz factor as a function of the detector time. The appropriate relations are given by the adiabatic energy equation (if the expansion is ultrarelativistic, the fireball cannot exchange energy with the ISM) and the photon arrival time:

$$E_0 = M(R)c^2W^2, \tag{4.2}$$

and

$$t_{obs} = \frac{R}{2cW^2}, \tag{4.3}$$

$M(R)$ and E_0 are the accumulated mass at a radius R and the value of the initial energy, respectively. With these equations in mind, and if the flux is parameterized in terms of its dependence on frequency and the time as $F_\nu \propto t^{-\alpha}\nu^\beta$ (Sari, Piran & Narayan 1998), a relation between α, β and p can be obtained. For the spherical adiabatic case this relation reads:

$$\alpha = \begin{cases} 3\beta/2 = 3(p-1)/4 & \text{for } \nu < \nu_c, \\ (3\beta - 1)/2 = (3p-2)/4 & \text{for } \nu > \nu_c. \end{cases} \tag{4.4}$$

4.1.4. Are GRBs Jet–like structures?

The aim of this section is to review the observational and theoretical evidence for a non-isotropic evolution of the GRBs or their afterglows. Actually, the present work tries to provide some answers to this question (see §4.3) in case of a particular astrophysical scenario (the collapsar model).

The possibility of non-isotropic emission is important for two reasons: the energetics and the event rate of the bursts. Clearly, beamed emission relaxes the energetic requirements to explain the observations. If the energy happens to be emitted into a solid angle Ω, the overall energy would be lower by a factor $\Omega/4\pi$ (if the angle is small, one can write $\Omega/4\pi = (1-\cos\theta)/2 \simeq \theta^2/4$). On the other hand, if the emission is beamed, we would not see all events (only those which point in our direction), *i.e.,* the actual event rate will be larger by $4\pi/\Omega$.

Beamed emission results both from an anisotropy of the emitting region and from relativistic beaming due to relativistic motion (see §3.3). The second effect produces an enhancement of the emission into a cone with an opening angle W^{-1} (if the source is moving towards us with a Lorentz factor W) independent of the shape of the emitting region. While beaming due relativistic motion is of the same strength in afterglows and in extragalactic jets (in both cases $W \sim 2-10$ implying $\theta_r \sim 0.1{-}0.5\,\mathrm{rad}$, θ_r being the angle of beaming of the radiation field, *i.e.,* $\theta_r \sim W^{-1}$), beaming of GRBs is much larger ($W \sim 200 \Rightarrow \theta_r \sim 10^{-2}\,\mathrm{rad}$). However, the beaming is determined by θ and not by θ_r, because a source will only be seen by those observers with a viewing angle up to θ from the center. Nevertheless, an observer can only see a fraction of the whole region of angular size W^{-1}, because the radiation is beamed at most into such an angle in his direction of observation. Furthermore, each of these fractions are causally disconnected (*e.g.,* Christiansen, Scott & Vestrand 1978; Shapiro 1979). The number of non-causally connected regions for a burst is $\sim (\theta W)^2$.[4] This number decreases with W, hence, during the afterglow there are fewer regions present than during the GRB, and when $\theta_r \sim \theta$ the external shock is coherent (*i.e.,* causally connected).

Can we, by any means, infer from observations the shape of the emitting region?. In particular, can we distinguish a spherical ejecta from a non-isotropic one?. Different authors have answered differently to these questions. Let us examine the alternatives in more detail. In the comoving reference frame of an expanding rela-

[4]Such number is calculated as $\dfrac{\Omega}{\Omega_r} = \dfrac{1-\cos\theta}{1-\cos\theta_r} \simeq \dfrac{\theta^2}{\theta_r^2} = (\theta W)^2$.

tivistic flow, the proper time required to reach a radial distance R (measured in the rest frame of the source) is R/cW (due to the contraction of the length in the direction of motion seen by the comoving observer). The maximum sideways expansion is not affected by the length contraction and, therefore it is R/W. As long as the Lorentz factor of the flow is sufficiently high ($W^{-1} < \theta$), the sideways expansion (R/W) is rather small, and according to PI99 matter does not have enough time to expand sideways and to realize that it is not part of a spherical shell.[5] Of course, as W decreases and $W^{-1} \approx \theta$ the communication between all points in the shell becomes causal and matter begins to expand sideways. The transversal expansion velocity is a matter of debate, because Sari, Piran & Halpern (1999) argue that as the matter at the front is constantly shocked to relativistic energies it should expand with the speed of light (*i.e.*, $\theta \sim W^{-1}$). Rhoads (1999) assumes that the sideways expansion occurs at the maximum allowed sound speed, $c/\sqrt{3}$ (*i.e.*, $\theta \sim W^{-1}/\sqrt{3}$). In any case, the sideways motion is so rapid that it dominates completely the fluid expansion. Narayan & Piran (1999) have found for an expansion into a homogeneous medium that[6]

$$W \propto R^{-3/2} \exp\left[-\frac{3}{2}\frac{c}{W_0\theta_0}\left(\frac{R^{3/2}}{R_0^{3/2}} - 1\right)\right] \tag{4.5}$$

where R_0, W_0 and θ_0 are the initial values of the radius, the Lorentz factor and the beaming angle respectively. The reduction of W, and the fact that the radiation is beamed into a larger cone ($W^{-1} > \theta_0$) reduces the observed emission and causes a break in the light curve[7]. After the break the emission decays faster (roughly by an additional factor t^{-1}). As the light curve changes, different relations between the spectral indexes α, β and p arise compared to the spherical adiabatic case (Eq. 4.4)

---

[5]This assertion can be formulated in hydrodynamical terms as follows: If one has an expanding jet with proper Mach number M_j then the opening angle of the beam is just $\sin\theta = \frac{1}{M_j}$. If the movement is highly relativistic, *i.e.*, $v_j \sim 1$, (even with the maximum allowed sound speed, $c_{s_j} = 1/\sqrt{3}$), it results that $M_j = \frac{W_j v_j}{W_{c_{s_j}} c_{s_j}} \sim W_j$ implying that $\theta \sim \frac{1}{W_j}$.

[6]Changing c in the exponential by c_s one gets Rhoads' (1999) solution.

[7]Panaitescu & Mészáros (1998) claim that two successive breaks will take place, one at $W \approx \theta_0^{-1}$, and a second one induced by the hydrodynamic time scale related with the sound speed at $W \approx (\sqrt{3}\theta_0)^{-1}$.

(see Halpern *et al.* 1999):

$$\alpha_{jet} = \begin{cases} 2\beta + 1 = p & \text{for } \nu < \nu_c, \\ 2\beta = p & \text{for } \nu > \nu_c. \end{cases} \quad (4.6)$$

There are many bursts (GRB 970228, 970508 and 980519) which do not show such a break in the light curve. However, Sari, Piran & Narayan (1999) interpret that this is because the sideways spreading must have started before the first optical observations. If this is true, using Eq. (4.3) PI99 finds an upper limit for the opening angle of $\theta < 0.05$ for GRB 980519.

The first direct evidence for a beaming break has been found in GRB 990123 (Kulkarni *et al.* 1999a) by a prompt optical detection. The optical afterglow exhibits three stages: (1) a prompt optical decay that Sari, Piran & Narayan (1999) interpret as coming from a reverse shock decaying like t^{-2} and disappearing quickly, (2) a subsequent afterglow decay proportional to $t^{-1.1\pm0.03}$, and (3) a late fast decline. The most likely explanation of this behavior is that we have observed the transition from a spherical like phase to a sideways expansion phase (Shari, Piran & Narayan 1999). From the transition time ($\sim$ 2 days) a beaming angle of $\theta_0 \sim 0.1$ is inferred. Additionally, the lack of a significant radio afterglow in GRB 990123 provides independent evidence for jet–like geometry (Kulkarni *et al.* 1999b). Most recently, Harrison *et al.* (1999) have seen such a transition 1.2 ± 0.08 days after the rising of GRB 990510 going from $t^{-0.82\pm0.02}$ to $t^{-2.18\pm0.05}$.

From all this evidence, it seems that GRBs most probably involve non-isotropic emission. However, the exact shape of the emission is far from being clear. Depending on the apparent geometry several more or less exotic terminologies are in use to describe the shape of GRBs: "jets", "bullets" or "pancakes". PI99 assumes that probably because of the analogy with AGNs jets the terminology "jets" has become the most widely used. However, typical extragalactic jets are long and narrow, and usually they show a continuous activity during $\sim 10^7 - 10^8$ years. Such time scales are much longer than the typical ones of the BHs that power them. A bullet shape, however, would be more self-consistent, because a bullet has a shorter length (in the direction of motion) and it clearly represents a transient phenomenon. Nevertheless, their angular sizes are $R\theta$ and their "lengths" are $L \sim cT$. Thus, if a burst of 30 s duration typically may have $L \sim 10^{12}$ cm, a radial size $R \sim 10^{13} - 10^{14}$ cm (see

§4.1.1) and $\theta \sim 0.1$, one finds $R\theta > L$. To PI99 such a source resembles a "pancake" moving relativistically in a direction perpendicular to its flat part. Moreover, if we look at its shape in the comoving frame it is longer by a factor W, *i.e.,* initially it is actually a bullet. However, even at this early phase the ejecta expands sideways proportionally to R (unless it is continuously collimated) and, consequently, even in the comoving frame it looks like a pancake.

4.2. Numerical simulations

The dynamics of spherically symmetric relativistic fireballs has been studied by several authors by means of 1D Lagrangian hydrodynamic simulations. Piran, Shemi & Narayan (1993) and Mészáros, Laguna & Rees (1993) have examined the expansion of a mass–loaded fireball, initially at rest, from the acceleration stage through the coasting phase. Panaitescu *et al.* (1997) have simulated the interaction between an expanding fireball and a stationary external medium with a uniform or power law density stratification, and Panaitescu & Mészáros (1998) computed the interaction between relativistically expanding shells. Kobayashi, Piran & Sari (1999) have studied the evolution of an adiabatic fireball expanding into a cold uniform medium. Using a 1D relativistic Lagrangian PPM code, Daigne & Mochkovitch (1999) and Daigne (1999) have studied the evolution of a relativistic wind with a very inhomogeneous distribution of the Lorentz factor. Such inhomogeneity produces internal shocks which may radiate reproducing the temporal variability of the observed bursts.

Other authors have studied the generation and transport of energy in potential astrophysical sources which might produce a relativistic fireball. In a sequence of papers Ruffert and coworkers (Ruffert, Janka & Schäfer, 1996, Ruffert *et al.* 1997; Ruffert & Janka 1998, 1999a) have used a Newtonian 3D Eulerian PPM hydrodynamic code (which includes self-gravity, the effects of gravitational wave emission and their back-reaction on the hydrodynamics, a neutrino leakage scheme and a realistic equation of state) in order to show that the neutrino emission associated with the dynamic phase of the merging or collision of two neutron stars, although being powerful, is too short to provide the necessary energy for GRBs by neutrino–

antineutrino annihilation (mainly because the accretion torus that forms due to the merger rapidly falls into the hole). Nevertheless, such a mechanism could explain the short GRBs (*i.e.,* those lasting less than 2 s; see Sect. 4.1). Ruffert and collaborators simulate the gravity of the BH by means of an effective Paczyński–Wiita potential and, in a post-processing stage, they evaluate the energy deposition by $\nu\bar{\nu}$ annihilation around the accretion torus.

MW99 have explored the evolution of rotating helium stars ($M_\alpha \gtrsim 10\, M_\odot$), whose iron core collapse does not produce a successful outgoing shock. Instead a BH is formed. For values of the specific angular momentum reasonable for such stars ($j \approx (0.3 \ldots 2) \times 10^{17}\,\mathrm{cm}^2/\mathrm{s}$) a compact accretion disk forms at a radius where the gravitational binding energy of the accreting stellar matter can be efficiently radiated as neutrinos. Assuming that the efficiency of neutrino energy deposition by $\nu\bar{\nu}$–annihilation is higher in the polar regions (because the $\nu\bar{\nu}$ cross-section is $\sigma_{\nu\bar{\nu}} \sim (1 - \cos\theta_{\nu\bar{\nu}})^2$, $\theta_{\nu\bar{\nu}}$ being the angle between the trajectories of the interacting neutrinos) MW99 obtained "relativistic" jets, along the rotation axis, which remain highly focused and seem to be able of penetrating the star. However, as they performed their simulations with a Newtonian hydrodynamic code, they got speeds in the jet flow which were appreciably superluminal, and they had to stop their simulations.

4.3. Relativistic jets from collapsars

The collapsar model of GRBs relies on the presence (or formation) of a fast rotating BH (of a few solar masses) surrounded by a thick accretion disk (torus) formed by the debris of a massive star which is not "instantaneously" accreted onto the BH essentially due the fast rotation of the progenitor star. This fast rotation also causes the formation of a "clean" axial funnel (*i.e.,* of relatively low density) centered around the rotation axis. The funnel favors the escape of the fireball, because it collimates and confines the fireball due to the much larger density of the walls of the funnel, and because it has a smaller baryon content. The expected result is the formation and evolution of a relativistic jet.

In the following we investigate some aspects of the collapsar model of MW99.

Using appropriate hydrodynamics (relativistic instead of Newtonian), a better description of the BH gravity (background Schwarzschild metric) and a variable gamma equation of state (which is less realistic than the one of Blinnikov, Dunina-Barkovskaya & Nadyozhin (1996) used by MW99; see §4.3.3) we have studied the question, whether it is possible to produce an ultrarelativistic jet releasing energy (at different deposition rates) near the center of the star in a region restricted to the neighborhood of the rotation axis.

4.3.1. Initial model and the numerical setup

Our axisymmetric relativistic simulations of jets from collapsars are based on Model 14A of MW99, which is obtained by MW99 in several steps. First, they evolve a $35\,M_\odot$ from the main sequence, without mass loss and rotation, to the presupernova stage (collapse velocity equal 1000 km/s) using a stellar evolution code. Then, they extract the helium core of the star which has a mass of $14.13\,M_\odot$, and remove its inner $2.03\,M_\odot$ which correspond to the iron core by introducing an inner boundary at a radius $r = 200\,\mathrm{km}$. In a third step, MW99 map the helium core model onto a 2D Eulerian grid and add some angular momentum to the spherical model, which is distributed so as to provide a constant ratio of 0.04 of centrifugal force to the component of gravity perpendicular to the rotation axis everywhere. Finally, MW99 evolve the model with a 2D hydrocode taking into account the effects of viscosity in the thick accretion disk (torus), which forms due to the action of rotation, by implementing the alpha viscosity prescription of Shakura & Sunyaev (1973) with $\alpha = 0.1$. At $t = 18.96\,\mathrm{s}$, when the central black hole, which forms in the center of the star, has acquired a mass of $3.762\,M_\odot$, we map the model to our computational grid.

In a consistent collapsar model the jet should be launched due to neutrino energy deposition by $\nu\bar{\nu}$–annihilation. Similar to MW99 we mimic this process by depositing energy at a prescribed (constant or variable) rate within a 30° cone around the rotation axis of the star[8]. In radial direction, the deposition region is bounded by

[8] Let us remind the reader that the numerical energy deposition may, in fact, be produced by any other physical mechanism like, *e.g.*, magneto-hydrodynamic processes. In this sense, our simulations

the inner boundary and an outer radius of $r = 6 \times 10^7$ cm. Numerically, the internal energy of the corresponding zones of the computational grid is raised to a certain value. Note that we thereby neglect any momentum deposition by $\nu\bar{\nu}$–annihilation.

We have investigated three different cases (Table 4.1): (i) a constant energy deposition rate of 10^{50} erg/s, (ii) a constant rate of 10^{51} erg/s, and (iii) a strongly (by a factor of ten) and rapidly (on milliseconds) varying energy deposition rate with a mean of value of 10^{50} erg/s. The first two cases roughly bracket the expected energy deposition rates of collapsar models, while the latter case mimics time–dependent mass accretion rates, *i.e.,* time–dependent $\nu\bar{\nu}$–annihilation, and hence a fluctuating energy deposition rate as found by MW99.

Name	# zones ($r \times \theta$)	$\dot{E}$ (erg/s)	Deposition rate	M (g)	η^{-1}
e50c043	200×43	10^{50}	constant	$(9 \pm 4) \cdot 10^{29}$	2.1 ± 1.9
e50c090	200×90	10^{50}	"	$(7 \pm 4) \cdot 10^{29}$	1.9 ± 1.7
e50c100	200×100	10^{50}	"	$(5 \pm 2) \cdot 10^{29}$	1.3 ± 0.9
e50v100	200×100	10^{50}	variable	$(7 \pm 2) \cdot 10^{29}$	1.9 ± 0.9
e50c180	200×180	10^{50}	constant	$(5 \pm 4) \cdot 10^{29}$	1.3 ± 2.0
e51c090	200×90	10^{51}	"	$(6 \pm 4) \cdot 10^{30}$	3.2 ± 3.1
e51c100	200×100	10^{51}	"	$(9 \pm 5) \cdot 10^{30}$	3.4 ± 3.4

Table 4.1: Overview of the simulated models at the end of the *pre–breakout* phase. Note that model names involving letters "c" or "v" refer to a constant or variable energy deposition rate $\dot{E}$, respectively. M is the jet rest-mass and η^{-1} is the baryon loading. The errors assigned to the mass are due to uncertainties in determining the material belonging to the jet (we consider that the jet is formed by the material whose velocity is larger than $0.1 - 0.3$ c, and whose specific internal energy density is larger than 5×10^{19} erg g^{-1}). The errors in the baryon loading are also caused by this uncertainty.

The simulations have been performed with GENESIS (see Chapter 2; and Aloy

may be representative of either a hypernova or a collapsar.

et al. 1999a) using 2D spherical coordinates (r, θ). In r–direction, the computational grid consists of 200 zones spaced logarithmically between the inner boundary at $r = 200$ km and the surface of the helium star at $r = 2.98 \times 10^{10}$ cm. Assuming equatorial symmetry we used four different zonings in angular direction: 43, 90 and 180 uniform zones (*i.e.*, $2^\circ, 1^\circ$ and 0.5° angular resolution), and 100 nonuniform zones covering the polar region $0^\circ \leq \theta \leq 30^\circ$ with 60 equidistant zones (0.5° resolution) and the remaining 40 zones being logarithmically distributed between $30^\circ \leq \theta \leq 90^\circ$. The latter mesh provides the same resolution than the 180 uniform zone run (Sect. 4.3.4).

As the equatorial region evolves slower than the polar one, the loss of resolution due to the logarithmic spacing in θ does not affect the main conclusions derived below. As the number of angular zones is reduced by almost one half compared to the model with 180 θ-cells, the computational costs are approximately reduced by one half, too. The typical size of a time step for this angular resolution is between tens of microsecond to some microseconds. Several million time step are required to follow the evolution of the system for several seconds.[9].

4.3.2. Equations of Special RHD in a spherical gravitational background

In order to take into account the BH's gravity, it has been necessary to include a spherical gravitational background field into GENESIS. Effects due to the self-gravity of the star on the dynamical evolution are neglected, *i.e.*, we consider only the potential generated by the BH (as if it were a point mass). The validity of such assumption relies on several facts:

- Deviations from spherical symmetry induced by the non-sphericity of the inner (and denser) matter distribution (the torus) are small, *i.e.*, a spherically symmetric potential provides a reasonably good approximation.
- The Newtonian gravitational potential of the system (BH + surrounding stellar

[9] Working with 8 processors on a SGI ORIGIN 2000 a typical simulation needs 1 to 2 weeks.

matter assuming a spherical matter distribution) differs by less than 20% from the potential produced by the central BH mass alone (see Fig. 4.1). The contribution of the stellar matter is negligible, even if the BH mass is smaller than the torus mass, which is distributed over a large volume).

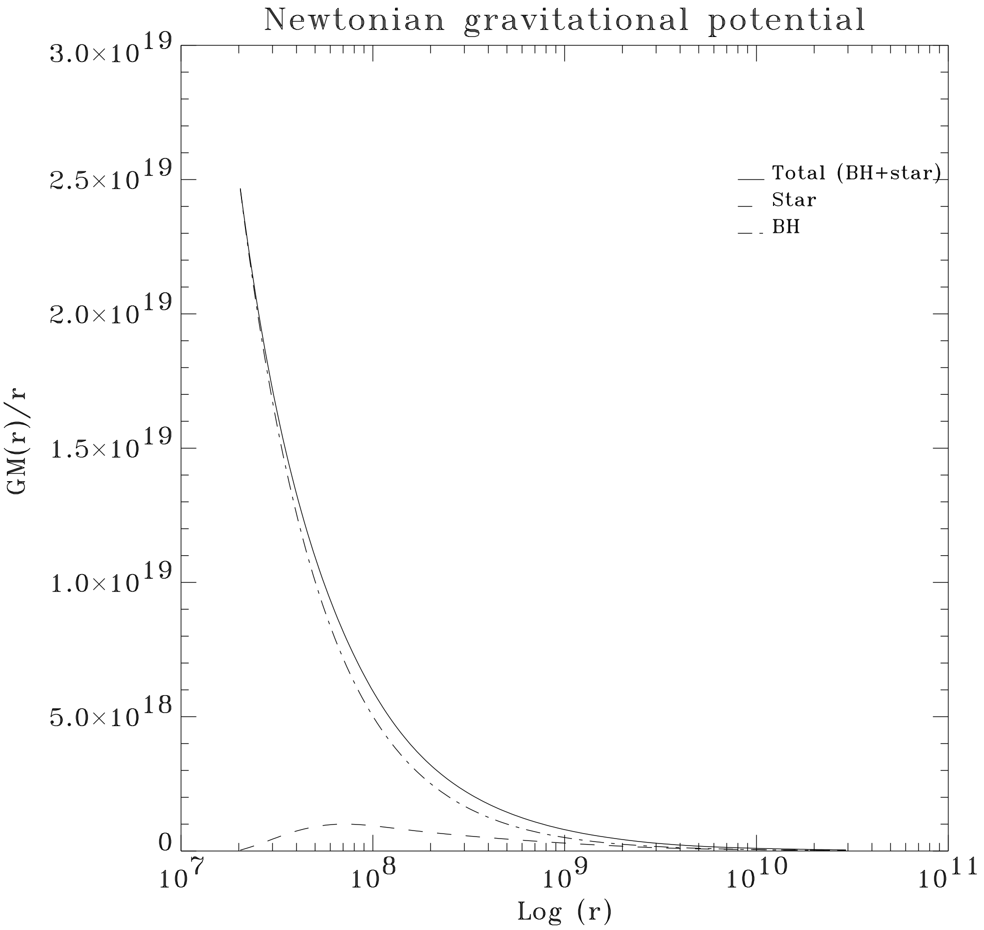

Fig. 4.1.— Newtonian gravitational potential of BH plus star (solid line), of the BH alone ($M(r) = M_{bh} = 3.763 M_{\odot}$; dotted-dashed line), and of the star alone (dashed line). The potential has been calculated assuming that the mass distribution is spherically symmetric (*i.e.*, $M(r)$ is the mass enclosed by an sphere of radius r), which is a good approximation to the real distribution.

The inner boundary of the computational domain (see §4.3.1) is at more than 35 Schwarzschild radii ($R_s = GM/c^2 \sim 5.6 \times 10^5$cm). General relativistic effects are small at such distances. Hence, although the star and the BH are rotating, it also does not make a large difference to represent the gravitational field of the BH by a static Schwarzschild metric instead of a more appropriate but also more complicated external Kerr metric. A more accurate treatment of General Relativistic effects becomes only necessary, if one comes closer to the event horizon.

The line element of the static Schwarzschild space–time can be written as (*e.g.*, Schutz 1985)

$$ds^2 = -e^{2\phi}dt^2 + e^{-2\phi}dr^2 + r^2 d\theta^2 + r^2 \sin^2\theta d\varphi^2, \tag{4.7}$$

where ϕ is a function only of r given by $e^{2\phi} = 1 - 2GM/rc^2$, or using natural units ($G = c = 1$) by $e^{2\phi} = 1 - 2M/r$. The evolution of a relativistic perfect fluid in this background is described by the following hyperbolic system of conservation laws:

$$\frac{1}{\alpha}\frac{\partial D}{\partial t} + \frac{1}{r^2}\frac{\partial}{\partial r}(r^2 e^{\phi} D v^r) + \frac{1}{r\sin\theta}\frac{\partial}{\partial \theta}(\sin\theta D v^\theta) + \frac{1}{r\sin\theta}\frac{\partial}{\partial \varphi}(D v^\varphi) = 0 \tag{4.8}$$

$$\frac{1}{\alpha}\frac{\partial S^r}{\partial t} + \frac{1}{r^2}\frac{\partial}{\partial r}(r^2 e^{\phi}(S^r v^r + p)) + \frac{1}{r\sin\theta}\frac{\partial}{\partial \theta}(\sin\theta S^r v^\theta) + \frac{1}{r\sin\theta}\frac{\partial}{\partial \varphi}(S^r v^\varphi) = e^{\phi}(-\frac{\partial \phi}{\partial r}(\tau + D) + \frac{1}{r}(2p + v^\theta v^\theta + v^\varphi v^\varphi)) \tag{4.9}$$

$$\frac{1}{\alpha}\frac{\partial S^\theta}{\partial t} + \frac{1}{r^2}\frac{\partial}{\partial r}(r^2 e^{\phi} S^\theta v^r) + \frac{1}{r\sin\theta}\frac{\partial}{\partial \theta}(\sin\theta (S^\theta v^\theta + p)) + \frac{1}{r\sin\theta}\frac{\partial}{\partial \varphi}(S^\theta v^\varphi) = \frac{1}{r}(\frac{\cos\theta}{\sin\theta}(p + S^\varphi v^\theta) - e^{\phi} S^\theta v^\varphi)) \tag{4.10}$$

$$\frac{1}{\alpha}\frac{\partial S^\varphi}{\partial t} + \frac{1}{r^2}\frac{\partial}{\partial r}(r^2 e^{\phi} S^\varphi v^r) + \frac{1}{r\sin\theta}\frac{\partial}{\partial \theta}(\sin\theta S^\varphi v^\theta) + \frac{1}{r\sin\theta}\frac{\partial}{\partial \varphi}(S^\varphi v^\varphi + p) = -\frac{S^\varphi}{r}(e^{\phi} v^r + \frac{\cos\theta}{\sin\theta} v^\theta)) \tag{4.11}$$

$$\frac{1}{\alpha}\frac{\partial \tau}{\partial t} + \frac{1}{r^2}\frac{\partial}{\partial r}(r^2 e^{\phi} \mathcal{A}^r) + \frac{1}{r\sin\theta}\frac{\partial}{\partial \theta}(\sin\theta \mathcal{A}^\theta) + \frac{1}{r\sin\theta}\frac{\partial}{\partial \varphi}\mathcal{A}^\varphi = -e^{\phi} S^r \frac{\partial \phi}{\partial r}, \tag{4.12}$$

with $\mathcal{A}^i = S^i - D v^i$.

In order to derive these equations, we have redefined the 3-velocity (and consistently the momentum) according to

$$v^j \;=\; \tilde{v}^j \sqrt{g_{jj}} \tag{4.13}$$

$$S^j = \tilde{S}^j \sqrt{g_{jj}},$$

where $\tilde{v}^j$ and $\tilde{S}^j$ are the velocities and momenta defined in §2.2 (note the change of notation). By this change the metric dependence is "hidden" in the contravariant components of the vectors. One has the relation

$$\mathbf{v} \cdot \mathbf{v} = \sum_{i=1}^{3} g_{ii} \tilde{v}^i \tilde{v}^i = \sum_{i=1}^{3} v^i v^i, \tag{4.14}$$

because the metric is diagonal. As all velocities are transformed into locally Minkowskian velocities, one can use Riemann solvers developed for Special Relativity without modification in General Relativity. Our approach only works for diagonal metrics. For a general metric the method Pons *et al.* (1998) must be applied, where a similar variable transformation is performed before calling the Riemann solver (and a corresponding back-transformation afterwards). We simply use the redefined variables.

Energy deposition by neutrinos is incorporated by an additional source term in the energy equation (4.13) of the form $\dot{e}dt$, where $\dot{e}$ is the deposition rate per unit volume, *i.e.*, $\dot{e} = \dot{E}/V_{\rm dep}$ (here $V_{\rm dep}$ is the volume of the deposition region). The energy is deposited uniformly within the deposition region. Both a constant and a variable deposition rate was considered (see Table 4.1).

4.3.3. Equation of State

The EOS is an approximation to the one used in Witti, Janka & Takahashi (1994) –they used a more accurate treatement of the pairs e^+e^-–. It includes the contribution of non-relativistic nucleons which behave as an arbitrary mixture of Boltzman gases, and the contribution of radiation together with an approximate correction due to pairs e^+e^-, *i.e.*, relativistic particles (photons, e^+ and e^-).[10] Complete ionization is assumed and the effects due to degeneracy are not included.

In order to calculate pressure, temperature (T), specific enthalpy, sound speed and $\left.\frac{\partial P}{\partial \varepsilon}\right|_\rho$ the local (baryonic) rest-mass density (ρ) and the energy density ($e = \rho\varepsilon$)

[10] The approximate expressions for the pressure and energy density of the pairs was derived by Janka & Takahashi (private communication). The corresponding entropy equation is given in Witti, Janka & Takahashi (1994).

have to be given. The expression for the pressure then reads:

$$p(\rho, T) = \frac{\mathcal{R}}{\mu}\rho T + \frac{1}{3}aT^4 + \frac{7}{12}aT^4 - \frac{7}{6}ab(T^2 - b\ln(1 + T^2/b)), \tag{4.15}$$

where $\mathcal{R}$ is the universal gas constant, a is the radiation constant, b is a combination of fundamental constants ($b = 5.3 \times 10^{18}\,\mathrm{K}^2$), and μ is the mean molecular weight per free particle (Cox & Giuli 1968)

$$\frac{1}{\mu} = \sum_i \frac{X_i(Z_i + 1)}{A_i}. \tag{4.16}$$

Here X_i are the mass fractions, Z_i the atomic numbers, and A_i the atomic masses of the ideal Boltzmann gases. The pair correction term accounts for the fact that electrons become non–relativistic (at sufficiently small densities) below $T \sim 5 \times 10^9\,\mathrm{K}$, and do not contribute much to the pressure ($\frac{7}{12}aT^4 - \frac{7}{6}ab(T^2 - b\ln(1 + T^2/b)) \to 0$ if $T^2 \to 0$ hence explicitly canceling the other correction term).

We have not considered nuclear reactions, *i.e.,* the initial composition at each point is only advected using the same technique as in Sect. 3.2.2 for the beam particle fraction. We advect nine nuclear species which are present in the initial model: C^{12}, O^{16}, Ne^{20}, Mg^{24}, Si^{28}, Ni^{56}, He^4, neutrons and protons.

Expression (4.15) gives the pressure as a function of ρ and T, while the hydrocode advances ρ and e. Hence, it is necessary to solve for the temperature iteratively (using a Newton–Raphson procedure) starting from an initial guess value for T:

$$e_g + e_r - e = 0, \tag{4.17}$$

e_g and e_r being the energy densities of the gas and the radiation (including pair correction), respectively. Both values are computed using the iterated value of the temperature, T_*:

$$\begin{aligned} e_g &= \frac{3}{2}\frac{R}{\mu}\rho T_*\,, \\ e_r &= aT_*^4\left(1 + \frac{7}{12}\left(\frac{4T_*^2}{b + T_*^2} - 1\right) + \frac{7}{6}ab(T_*^2 - b\ln(1 + T_*^2/b))\right). \end{aligned}$$

Once equation (4.17) has been solved for T up to a prescribed tolerance, the value of p can be computed from (4.15) using the density. Next the specific enthalpy

$(h = 1 + \varepsilon + p/\rho)$ is calculated, and finally the sound speed is obtained by

$$c_s = \sqrt{\frac{p\gamma}{\rho h}},$$

$$\gamma = \left.\frac{d\ln p}{d\ln\rho}\right|_s = \frac{\frac{p^2}{e} + p_g}{p},$$

where p_g is the pressure contribution of the nucleons ($p_g = (\mathcal{R}/\mu)\rho T$), and s is the specific entropy.

Finally, for the Riemann solver one needs the value of the derivative $\left.\frac{\partial p}{\partial \varepsilon}\right|_\rho$, which is obtained from

$$\begin{aligned}
\left.\frac{\partial p}{\partial \varepsilon}\right|_\rho &= \rho \left.\frac{\partial p}{\partial T}\right|_\rho \left(\left.\frac{\partial e}{\partial T}\right|_\rho\right)^{-1}, \\
\left.\frac{\partial p}{\partial T}\right|_\rho &= \frac{R}{\mu}\rho + \frac{1}{3}aT^3\left(11 - \frac{7b}{b+T^2}\right), \\
\left.\frac{\partial e}{\partial T}\right|_\rho &= \frac{3}{2}\frac{R}{\mu}\rho + 4aT^3\left(\frac{17}{12} + \frac{7}{2}\frac{T^2}{b+T^2}\left(1 - \frac{1}{3}\frac{T^2}{b+T^2}\right) - 1\right) + \frac{7}{3}ab\frac{T^3}{b+T^2}.
\end{aligned}$$

4.3.4. Constant and moderate energy deposition rate

The first case we have considered has a constant energy deposition rate of 10^{50} erg/s. Although this rate is only moderate, concerning collapsar models, a relativistic jet forms within a fraction of a second and starts to propagate along the rotation axis. In Figs. 4.2 and 4.5 the evolution of the rest-mass density and the Lorentz factor are plotted in eight snapshots from the initial state (panel (a)) to the last computed model (panel (h)). From these figures one can notice that all the morphological elements of the BR74 jet model are present: the terminal bow shock, a narrow cocoon, a contact discontinuity between the star and the jet itself, a faint hot spot (noticeable in Fig. 4.3), etc. The propagation of the jet is unsteady, because of density inhomogeneities in the star, particularly along the axis. For example, Fig. 4.2c shows the combined effect of matter being piled up (in front of the jet) and of a locally increasing stellar density. This gives rise to a "split" of the head of the jet along with a head deceleration and a cleaning of the central channel. The density inside the jet flow drops considerably with time reaching values as low as $\sim 10^{-6}$ g/cm^3 (Fig. 4.4). The density profile within the jet (Fig. 4.4) shows large variations (up to a factor of 100) due to internal shock waves, which can be identified when comparing density and pressure distributions at the same time (Figs. 4.2 and 4.3). Some of the internal shocks are of biconical nature recollimating the beam. These shocks develop during the jets propagation through the star. Additional shocks may appear in the subsequent jet evolution playing the rôle theoretically assigned to the "internal shocks" in the emission processes (see Sect. 4.1.1).

Fig. 4.2 shows that the density structure of the star does not change noticeably during the whole evolution. This statement also holds for other variables (Figs. 4.2 – 4.6), and hence proves that the evolution time scale of the jet is short compared to the (dynamical) time scale required to change the mass distribution within the star. This result, a posteriori, justifies our treatment of the gravity of the star (see Sect. 4.3.2).

The Lorentz factor of the jet continuously increases with time, but it grows non-monotonically (Fig. 4.7). The maximum Lorentz factor is not reached in the head of the jet (which propagates at a mean speed of 7.8×10^9 cm/s, or $W \sim 1.04$), but in the rarefaction waves that form behind the biconical shocks. A particularly strong recollimation shock wave forms during the early stages of the evolution (after the initial transient state). This shock moves outwards, and reaches a distance of $\sim 10^{10}$ cm in the final model (Fig. 4.2h). A very strong rarefaction wave behind this recollimation shock causes the largest local acceleration of the beam material.

Due to the energy deposition and the dropping density, the specific internal energy becomes extremely large within certain parts of the jet, reaching 10^{28} erg/g in some small regions near the rotation axis at radii less than 10^8 cm. The mean value of ε is $\sim 10^{20} - 10^{21}$ erg/g, or $\sim O(c^2)$ (Fig. 4.8), *i.e.,* the jet is very hot. A mean temperature of $\sim 5 \times 10^8$ K can be estimated from Fig 4.6 implying that its pressure is radiation dominated, in accordance with the simplified EOS used in our simulations. Clearly, the EOS used in MW99 is more realistic, particularly in the denser regions of the torus. But as the jet does not propagate through such regions and as the torus does not evolve significantly from its initial state, the usage of a simplified EOS should not be problematic.

The relativistic treatment of the hydrodynamics leads to a overall qualitatively

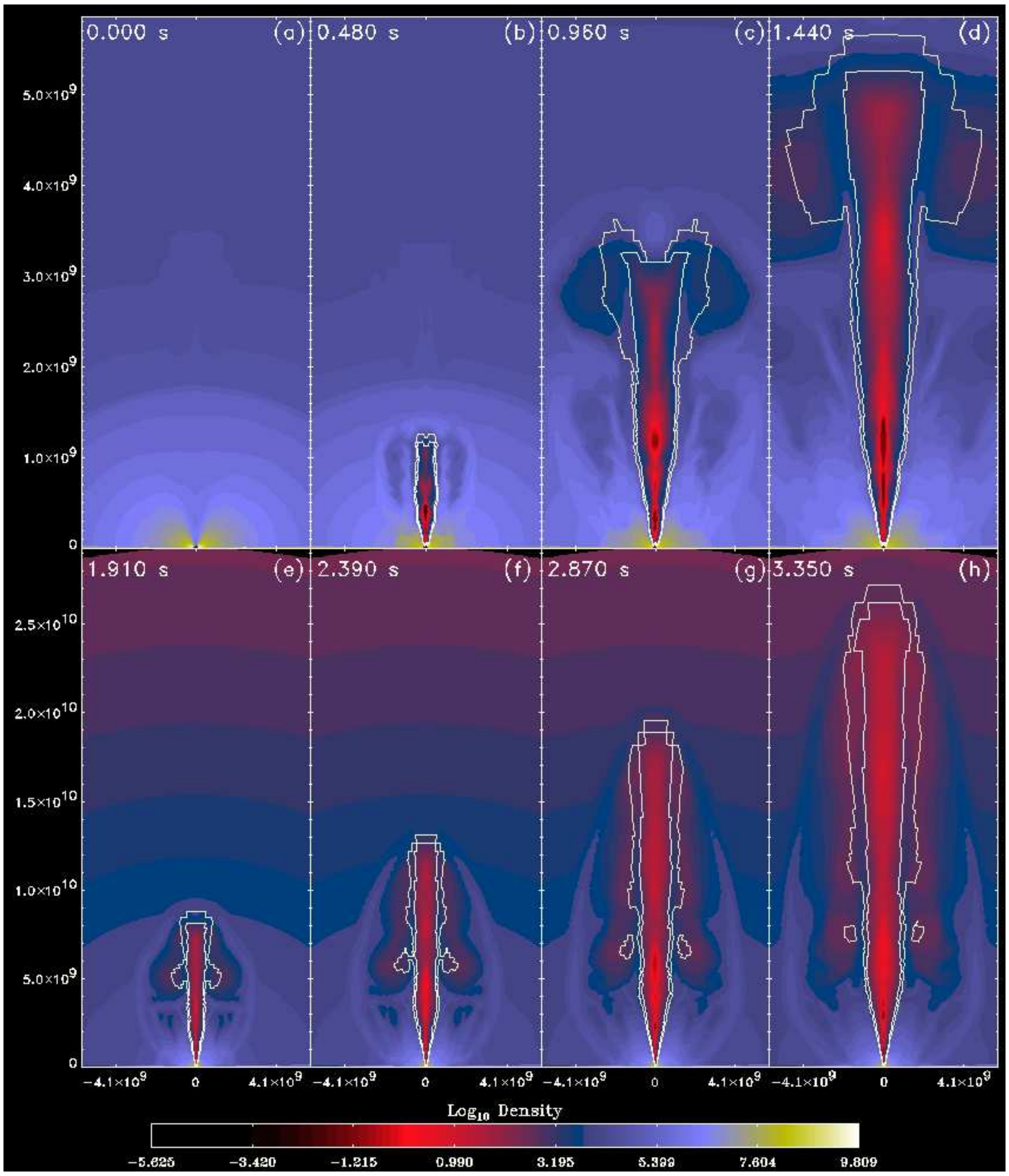

Fig. 4.2.— Color contour maps of the logarithm of the rest–mass density distribution at different evolution times (model e50c100). All the units are given in CGS system. Snapshots are arranged by rows and from left to right corresponding to different evolutionary times (marked in the top left corner of each panel). The panels in the top row have been zoomed by a factor five compared to those in the bottom row to exhibit more details. The two white isocontours correspond to the "limits" of the jet considering two different criteria: the inner contour assumes that the jet is formed by material with $\varepsilon \geq 5 \times 10^{19}$ erg/g and $v_r \geq 0.3c$; the outer contour represents the part of the system with $\varepsilon \geq 5 \times 10^{19}$ erg/g and $v_r \geq 0.1c$.

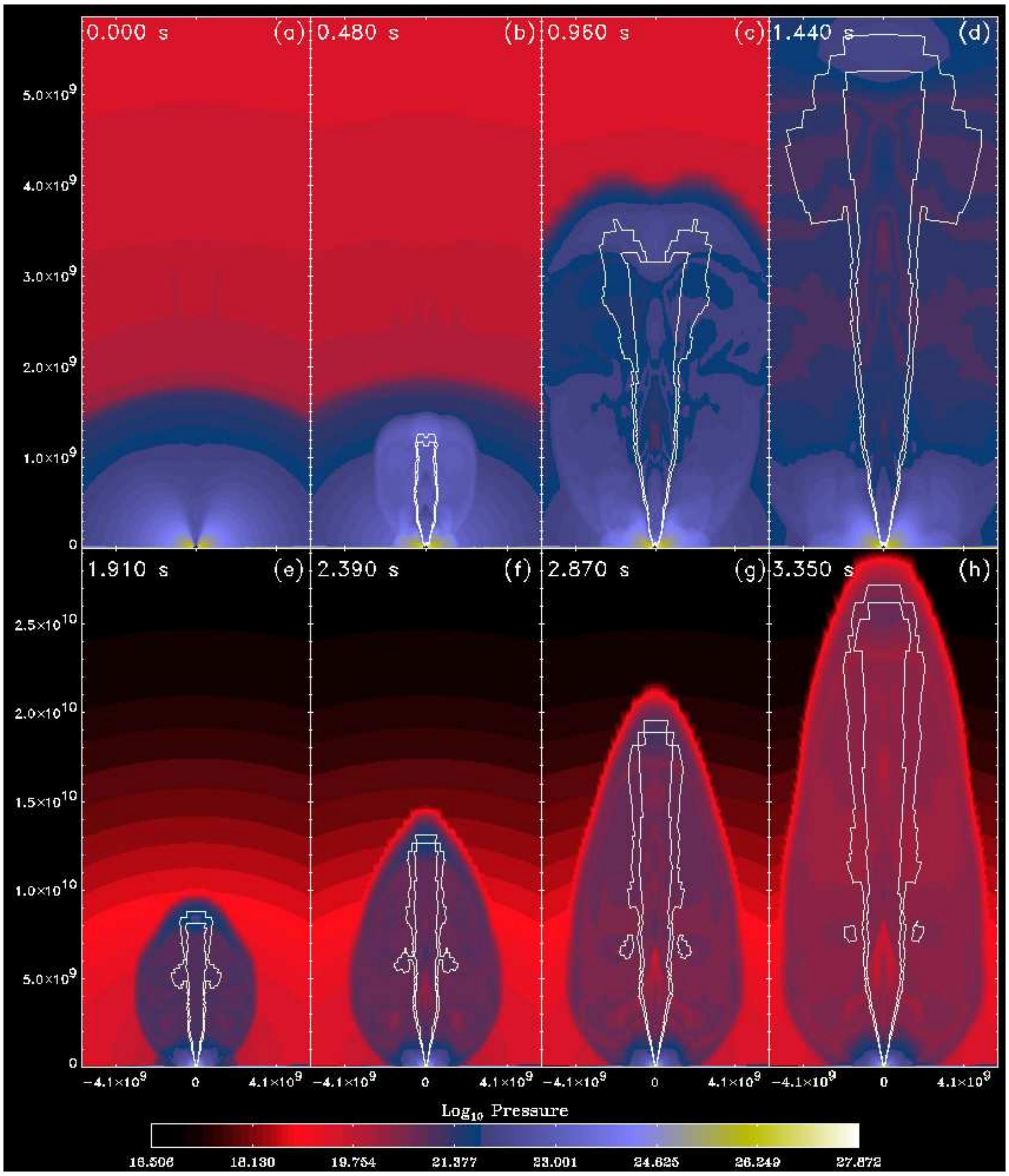

Fig. 4.3.— Same as Fig. 4.2, but showing the logarithm of the pressure distribution.

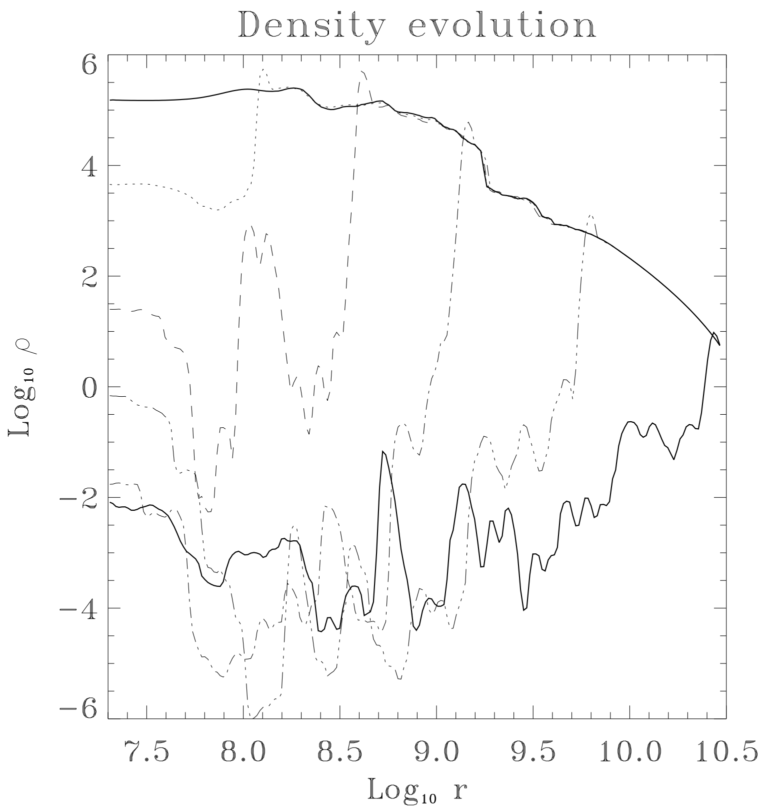

Fig. 4.4.— Evolution of the rest–mass density along the polar axis for several epochs of model e50c100. From top to bottom the different line styles are associated to the times: 0.00, 0.03, 0.13, 0.50, 1.5, and 3.35 s, respectively.

quite similar (formation of a jet), but quantitatively very different evolution than in MW99, although the energy deposition rate of MW99 is the same than ours. As one can read off from their Fig. 27, the jet has propagated 7,000 km within the first 0.824 s. Using the jet's energy density, MW99 infer from this fact a Lorentz factor of the matter of ~ 10. Furthermore, they find a half opening angle for their jet of $10°$. In our simulation, at the same time for the same angular resolution ($\sim 2°$) and the same energy deposition rate (10^{50} erg/s) the head has reached a radius of 30,000 km (4.3 times farther out than in MW99), but its maximum Lorentz factor is only 4.62 (less than half than in MW99) located in a blob at $\sim 12,200$ km. Moreover, in our model another blob of matter moves with a speed of $W \simeq 3$ at a radius of $\simeq 20,000$ km. Our half opening angle is $6°$, *i.e.,* it is roughly half of that of MW99.

Another important issue, that was not analyzed by MW99, is the dependence

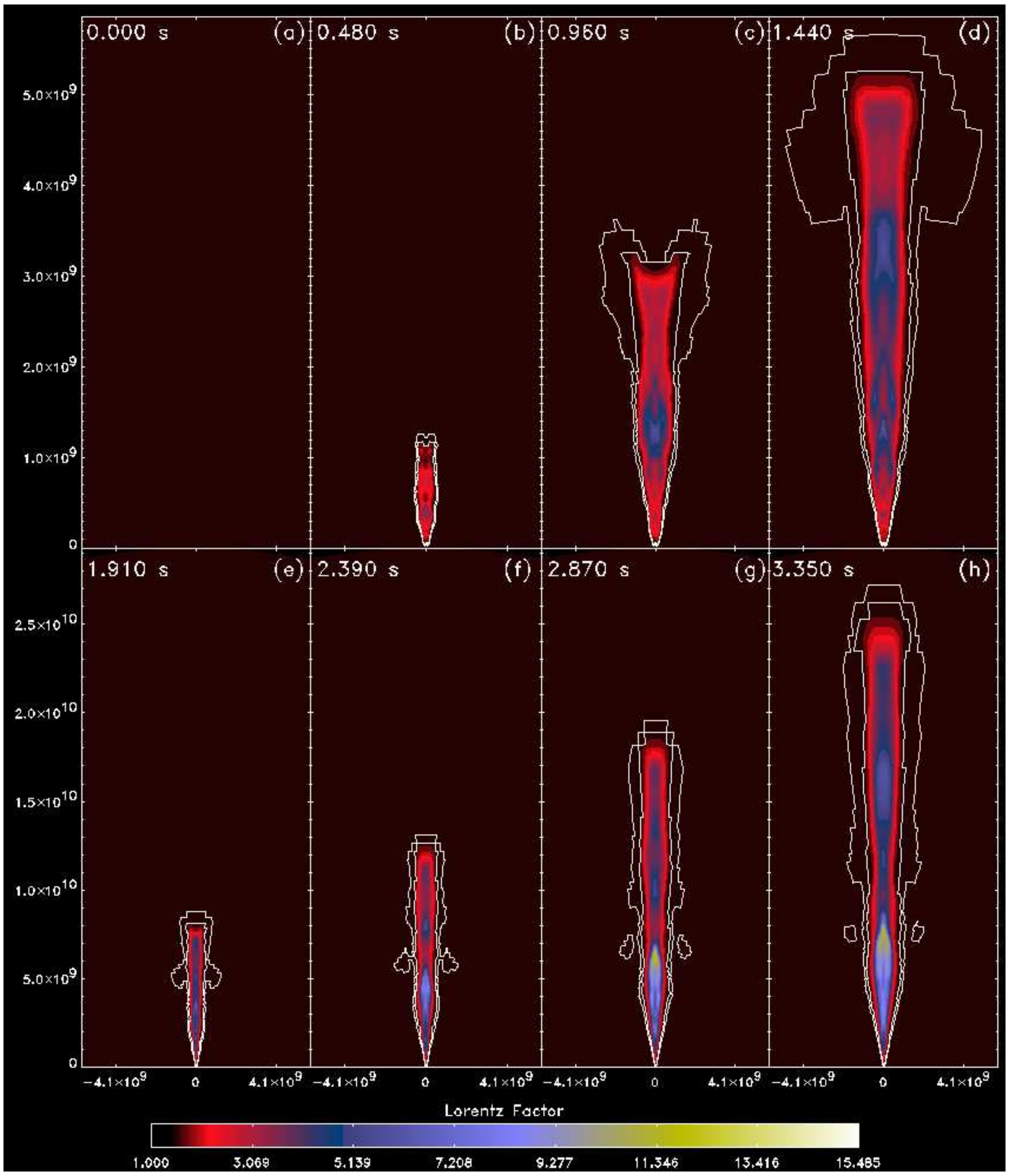

Fig. 4.5.— Same as Fig. 4.2, but showing the distribution of the Lorentz factor.

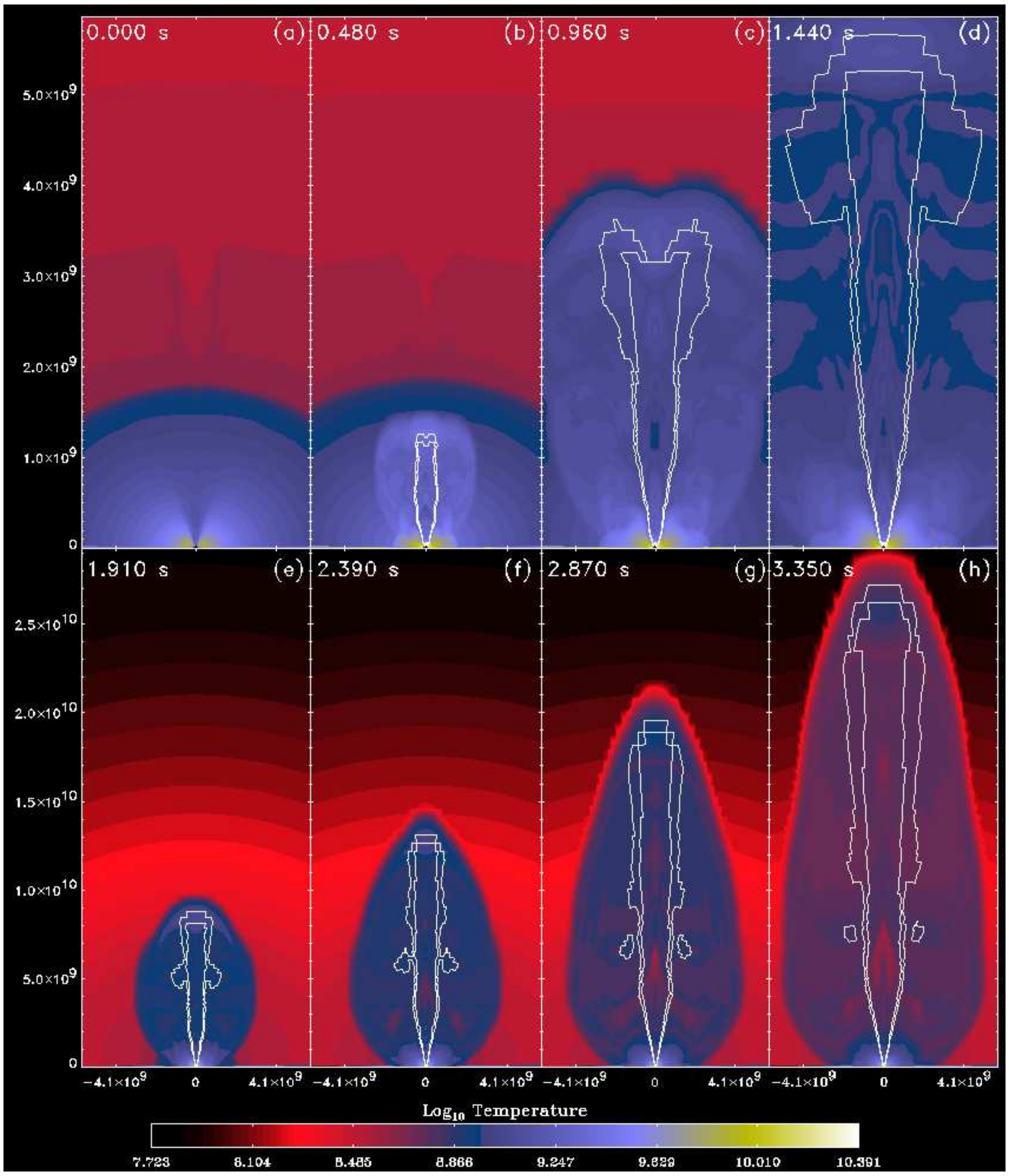

Fig. 4.6.— Same as Fig. 4.2, but showing the logarithm of the temperature distribution.

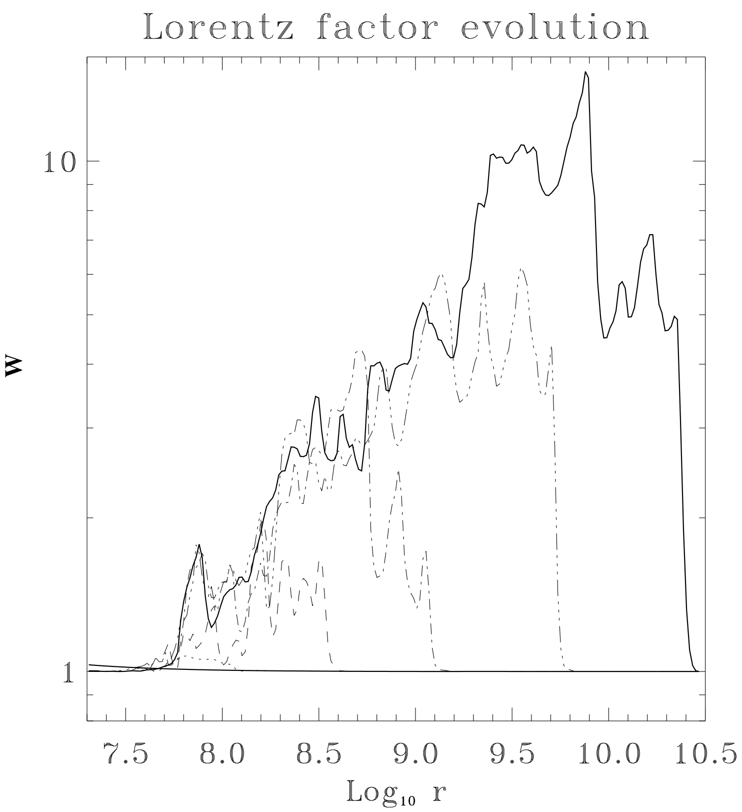

Fig. 4.7.— Evolution of the Lorentz Factor along the polar axis for several epochs of model e50c100. From top to bottom the different line styles are associated to the times: 0.00, 0.03, 0.13, 0.50, 1.50 and 3.35 s.

of the results on the grid resolution. We have investigated the dependence of the results on the angular resolution (for a fixed radial grid). Table 4.2 shows that we find significant changes with resolution. For instance, the radius reached by the head of the jet after 0.82 s varies by about 30% when increasing the angular resolution by roughly a factor of four. The propagation speed tends (non-monotonically) towards a value $W_{\max} \approx 4.4$ as the angular grid resolution is increased. A similar comment holds for all hydrodynamic variables. Generally speaking, models e50c100 and e50c180 are very similar globally, even though the local values of the maximum specific internal energy or the minimum density are quite different. This result is not unexpected, because the resolution of both models is the same near the axis (along which the jet is propagating).

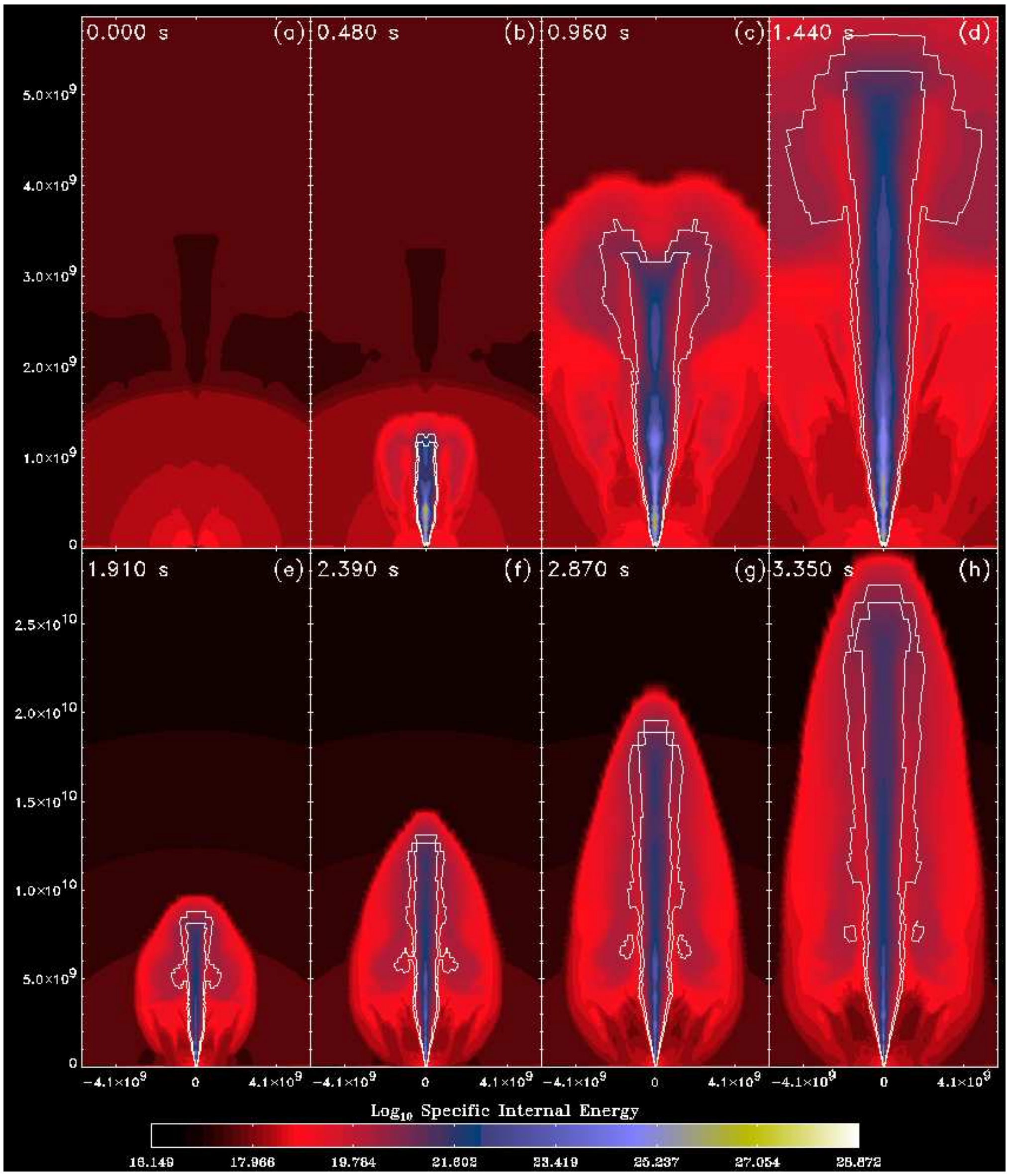

Fig. 4.8.— Same as Fig. 4.2, but showing the distribution of the logarithm of the specific internal energy density.

Thus, we need an angular resolution four times larger than that of MW99 to reach acceptable numerical convergence. When comparing our results with those of MW99 the question arises to what extent are their results dominated by numerical resolution and to what extent by their different input physics (realistic EOS, Newtonian self-gravity of stellar matter, etc). This problem should be kept in mind in the following discussion.

We are going to discuss now some general trends that can be inferred from the dependence of the results on the resolution (considering the simulations up to 3.35 s).

Model	Distance (km)	$W_{\rm max}$	θ (deg)	$\rho_{\rm min}$ (g/cm^3)	$\varepsilon_{\rm max}$ (erg/g)
e50c043	30,000	6.03	8	2.35×10^{0}	3.38×10^{23}
e50c090	27,000	3.92	8	2.37×10^{-3}	1.53×10^{27}
e50c100	26,000	4.62	6	4.33×10^{-4}	1.36×10^{27}
e50c180	22,000	4.40	7	1.38×10^{-4}	6.14×10^{27}

Table 4.2: Some characteristic quantities obtained for models with an energy deposition rate of $\dot{E} = 10^{50}$ erg/s for different grid resolution at time 0.820 s. Distance gives the radius of the head of the jet, and $W_{\rm max}$ and $\varepsilon_{\rm max}$ are the maximum Lorentz factor and specific internal energy at this time. $\rho_{\rm min}$ is the absolute minimum value of the density. The values of θ are measured with an accuracy of 1°.

The highest specific internal energy is concentrated in small blobs at radii less than 5×10^8 cm. These blobs are connected by a narrow central channel (which gets narrower when the resolution is increased). The average specific internal energy within the jet is $\sim 10^{21}$ erg/g in almost all models. The presence of the central channel could be a numerical artifact (*e.g.*, a *wall heating* effect like that mentioned in Chapter 2, Sect. 2.4.2) related to the reflecting boundary condition along the axis.

At the beginning of the simulations the half opening angle lies in the range $6° - 8°$ which is smaller than 10° (MW99 value). Moreover, the opening angle shrinks from $8°$ to $6° - 7°$ when the resolution is increased. Later in the evolution (at $\sim$ 1.5s) a strong recollimation shock reduces the opening angle to less than 1°. This effect is most remarkable in those models having the best resolution. Consequently, the strong collimation found by us cannot be definitely ascribed to relativistic effects alone, because insufficient grid resolution might play some rôle.

During the late stages of the jet propagation the distance reached by the head of the jet tends to differ slightly (Fig. 4.9), while during the initial stages of the evolution, all models follow very similar evolutionary tracks. This can be explained by the non-linearity of the hydrodynamic equations, which may amplify differences present in the initial models (produced by the interpolation of the initial model of MW99 onto our different computational grids).

When the resolution is increased and becomes sufficiently good, $W_{\rm max}$ approaches a value of $\sim 15 - 20$ (at shock break out), the maximum value being reached at a radius $\sim 8 \times 10^9$ cm. The value of $\rho_{\rm min}$ is quite sensitive to the resolution. It drops to a value of about $5 \times 10^{-6}\,{\rm g/cm^3}$ in the highest resolution run. However, as the density minima are located near the axis (in the first θ-zone), they may be affected by numerical errors. Another much better indicator of the convergence behavior of the code is the mean density in the jet[11] which always lies in the range $10^{-2} - 1\,{\rm g/cm^3}$. In addition, the final maximum density ($\sim 5 \times 10^8\,{\rm g/cm^3}$) is always obtained at a radius of $\sim 3 \times 10^7$ cm within the torus. Hence, even if the point values are not exactly the same, the global maximums and minimums can be found in the same regions. This result also confirms that outside the axial cone resolution does not play an important rôle. Nevertheless, if one wants to include neutrino generation and transport processes from the torus into the simulations, and wants to model the accretion from the torus, a better resolution near the equator is crucial (because this region has the highest accretion rate, see below).

The structure of the jet is characterized by shocks and knots with a varying number of blobs of high W and low density. As one expects, the morphology of the jet is richer at better resolution. It shows a narrow spine of low density connecting the various blobs.

The mean temperature in the jet, $\bar{T}$, is (in all models) $\sim 5 \times 10^8$ K. The max-

[11]This indicator is better because it refers to a global property.

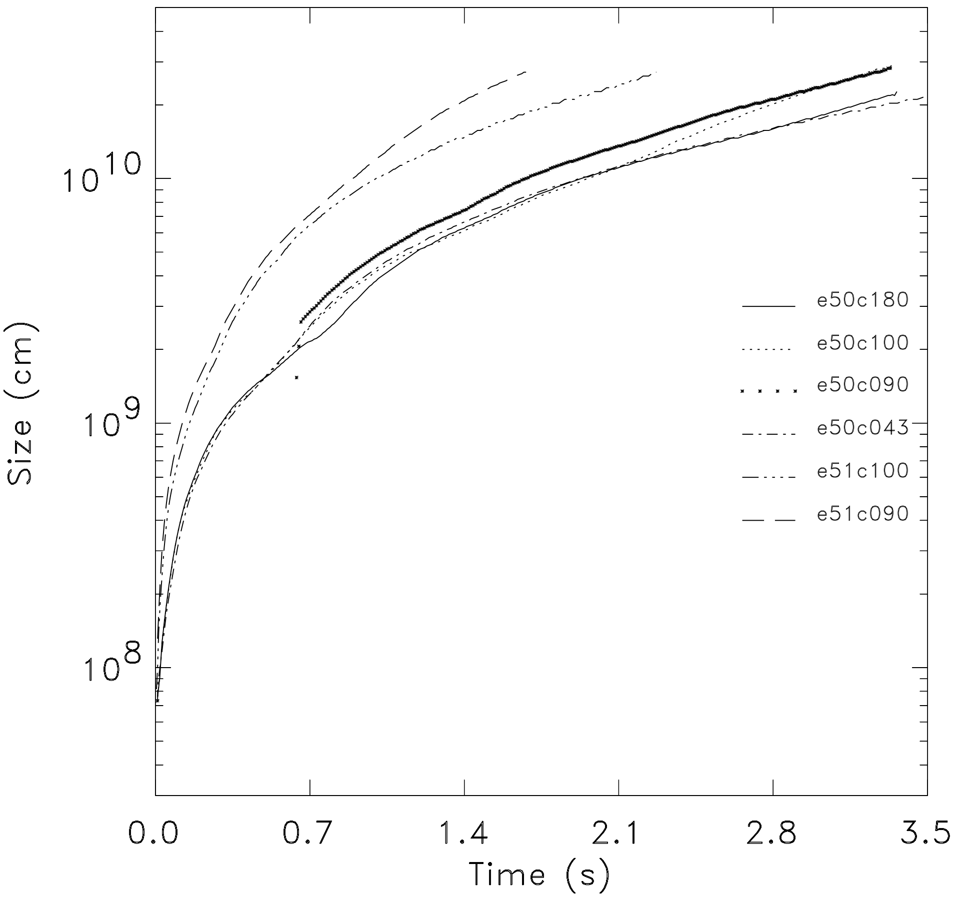

Fig. 4.9.— Evolution of the head position for models with a constant energy deposition rate equal to 10^{50} erg/g. For model e50c090 the available data only cover the interval $[0.7, 3.35]$ s.

imum temperature in the computational domain, $T_{\rm max} \sim 2.3 \times 10^{10}$ K, is always attained at the central part of the torus. This temperature value implies that our calculations are self-consistent, because even when we deposit energy to heat up the matter, its temperature does never exceed the temperature of the emission region (*i.e.,* the walls of the torus). Moreover, the temperature is well below the pair creation threshold and is compatible with the assumed temperature of the GRB emitting region (a few keV, see Sect. 4.1.1).

The baryon mass enclosed by the jet and its cocoon is about $10^{-4} M_{\odot}$. This value is large compared with the expected mass of the ejecta in a typical GRB ($\sim 10^{-6} M_\odot$; Rees 1997). It does prevent the formation of a GRB, mainly because in later stages of the evolution new mass will be piled up in front of the expanding jet. Our results show an alternative to the standard model, which is that instead of having a thin shell of matter expanding ultrarelativistically (what requires a low enclosed mass), one has an expanding bubble with an inner jet-like ultrarelativistic core that would be the responsible of the gamma-ray emission (once the bubble becomes optically thin). Such a picture is similar to what is assumed valid for extragalactic jets, in the sense that the head propagation speed (and the sideways expansion) is subrelativistic or mildly relativistic, while the beam itself is relativistic (even at kpc scale) and the main responsible for the synchrotron emission. Actually that situation might even allow for interesting observational implications; for instance, one can imagine that the dense slow matter is iron group matter irradiated by gammas from the beam behind it. This may produce iron lines as indicative in some jet sources (which do not make a GRB because of the orientation of the source relative to an Earth observer.

Mass accretion is slowed down or even stopped by the deposition of energy. The flow of stellar matter across the inner boundary (*i.e.*, the flow of mass that eventually ends up in the black hole) is almost stopped after $\sim 0.15\,\mathrm{s}$ when $\sim 1 M_\odot$ has been passed the inner boundary (see Fig. 4.10). The accretion rate is highly variable on time and depends on latitude too. The largest accretion rate is observed in the equatorial layers of the star (between 60° and 90°), because they are the most dense ones (due to the presence of the torus with densities above $10^8\,\mathrm{g/cm^3}$). The accretion rate decreases with angle, and reaches a minimum in a cone of $\sim 10^\circ$ around the axis, because the polar regions initially have the smallest density and the energy deposition promptly stops the accretion there. One can notice from Fig. 4.10 that there is a change in the slope of the accreted mass around $\sim 1.2\,\mathrm{ms}$, which must be a result of (1) the numerical relaxation of the initial model and (2) the energy deposition itself. The effect (1) is due to the interpolation necessary to produce our initial model from data which have been produced by a different code using other EOS and that includes effects such as α-viscosity of the accretion disk. The effect (2) is produced because, initially, the energy deposited is used to heat up the innermost region of the star increasing its pressure, and thereby preventing fast accretion. This effect is smaller and delayed in equatorial regions (see the dotted line in Fig. 4.10 up to a latitude of $63.8° - 90.0°$), which contributes to the accreted mass up to ~ 0.15 s because it is farther from the deposition volume. The outermost shells of

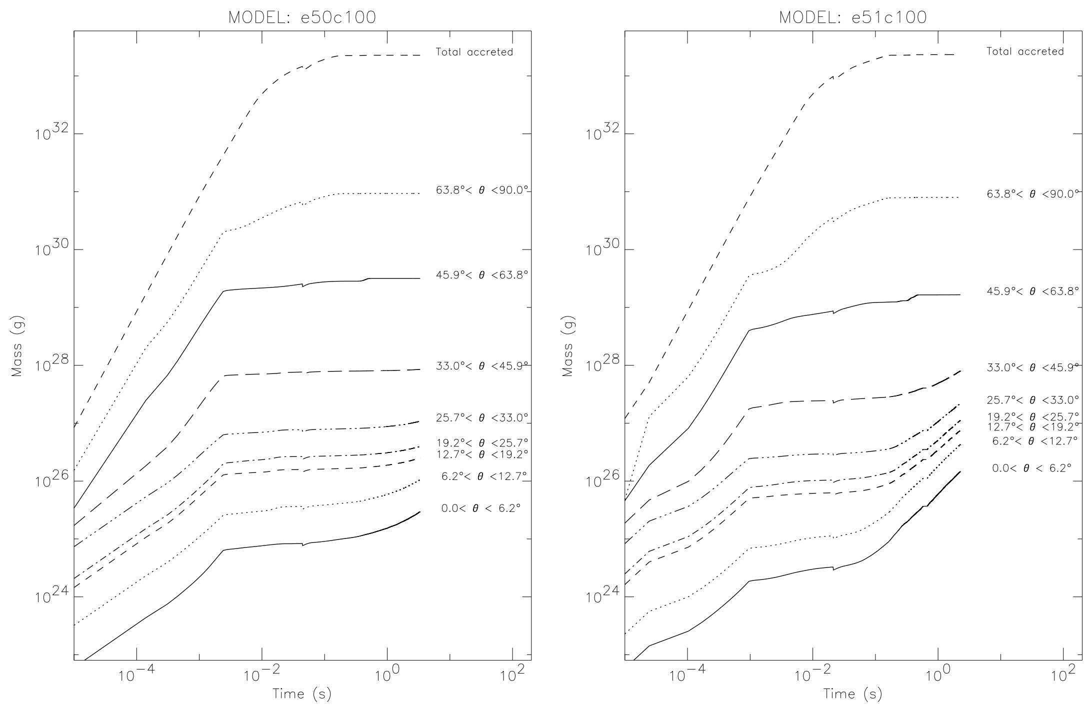

Fig. 4.10.— Time evolution of the cumulative mass that is lost across the inner boundary at different latitudes for models e50c100 (left) and e51c100 (right), respectively.

the star are falling with velocities as small as 10^{-6}c, *i.e.*, a negligible amount of mass ($1.7\times10^{-4} M_{\odot}$) is entering the computational grid through the outer boundary. From an analysis of the radial velocity field at the end of the simulations (see Fig. 4.11 which corresponds to model e50c180, but it is representative of the other models, too) we have found that there exists an extended torus-like region centered around the equator having a velocity ≈ 0. In Fig. 4.11 this region is surrounded by the isocontour where the velocity is equal to zero. Note that the region is not connected to the central torus, because in between (and around the jet cavity –like in MW99–) a layer of infalling material is present. The maximum infall velocity depends on resolution, and lies, in the best resolution run, in the interval $0.357c$ - $0.398c$, while for the lowest resolution the value is $0.097c$. These maximum velocities are found around the central torus.

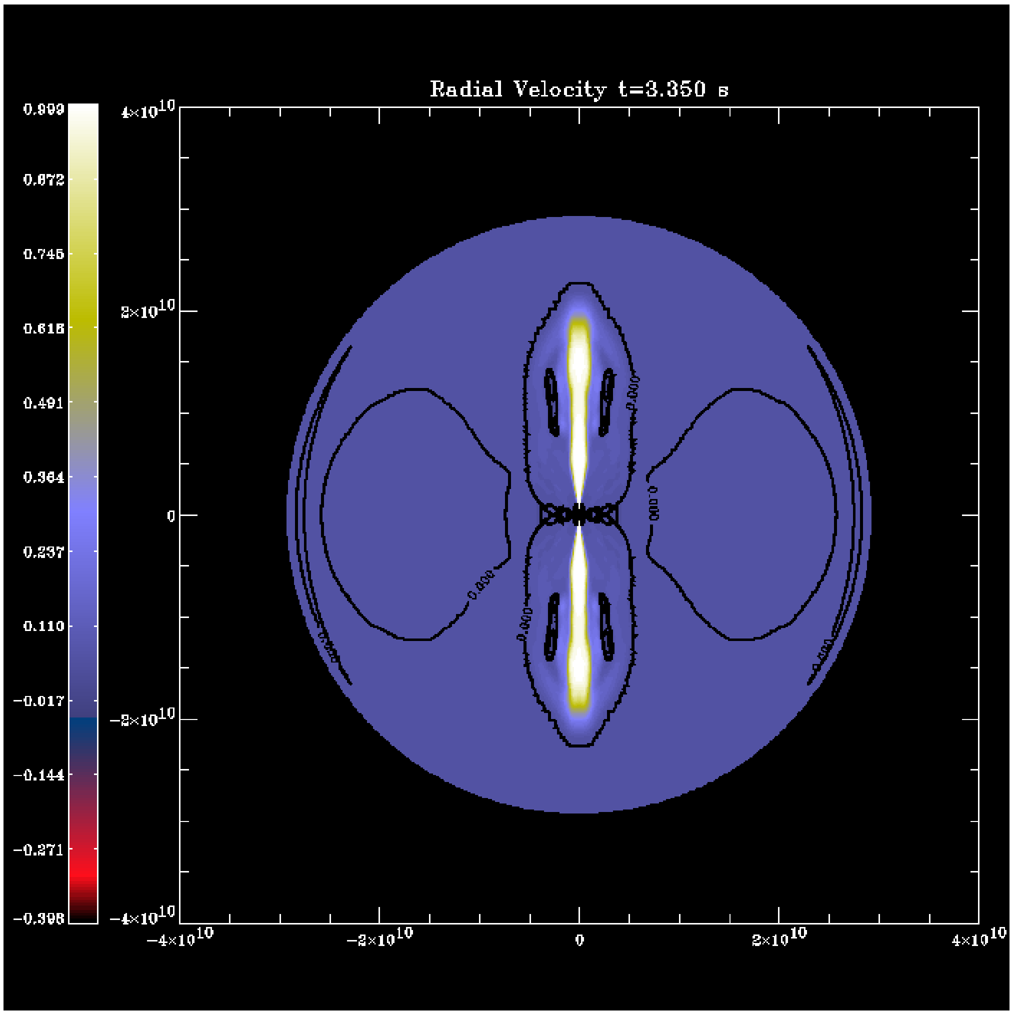

Fig. 4.11.— Snapshot of the radial velocity of model e50c18 at the end of the simulation (at t=3.35 s). Isocontours correspond to velocity values -0.05c, -0.01c and 0, respectively. Numbers at the X and Y axes give the distance in centimeters.

The baryon load of the jet has been calculated for each model (see Table 4.1) as the ratio of (the approximate value of) the jet mass to the energy deposited. The extraction of the values involves some uncertainty, because there exists some arbitrariness in measuring the jet mass accurately.[12] The baryon load is very similar for the four cases we have studied. It seems to decrease with increasing resolution, although the uncertainties are so large that all models with a deposition rate of 10^{50} erg/s show a baryon load consistent with that of the highest resolution run of $\eta^{-1} \simeq 1.3$. The explanation is simple. Models with the a worse resolution have larger computational cells. Hence, the determination of the jet shape is less accurate, *i.e.,* some cells may include material that does not belong to the jet. This happens for those cells located at the jet boundary.

The value of the baryon contamination found in the simulations is not compatible with that assumed in the standard model (see Sect. 4.1.1). However, such a model considers an isotropic relativistic expansion into a uniform external medium. In our case, neither the expansion is isotropic nor the external medium is uniform. In fact, depending on the criteria employed to *define* the jet, there are regions inside the beam where $\eta^{-1} \lesssim 10^{-3} - 10^{-5}$ (precisely where the Lorentz factor is larger). Additionally, the mass entrained into the jet increases slower with time than the energy released, because once the funnel is evacuated mass entrainment across the jet boundary almost seizes (of course this argument depend on resolving the KH instabilities on the jet funnel). In fact, considering the evolution of η^{-1} for model e50c100 after jet breakout (Sect. 4.3.7), we find a decrease of the baryon load by a factor of four in less than 1.8 s. If this decrease continues in time, a value of $\eta^{-1} \sim 10^{-3}$ is reached in less than 9 s.

4.3.5. Constant large energy deposition rate

In order to investigate the effect of the deposition rate on the overall evolution two runs have been made with a tenfold increased energy deposition rate, e51c090 and e51c100, which differ in grid resolution (Table 4.1). We find that a resolution of 90 θ-zones is insufficient to capture accurately all relevant features. In addition, some numerical problems were encountered in model e51c100. The main reason for these

[12] The jet is not well defined, because we do not have a conserved variable that unanimously identifies jet matter. This situation is different in the case of extragalactic jets, where the beam mass fraction allows us to properly locate the jet boundary (neglecting effects of numerical diffusion).

problems is the artificial way in which the energy is released in the computational domain. In reality, the energy deposition of the neutrinos is smoothly distributed over the whole star, but it is strongly peaked near the axis and close to the star's core. In the previous simulations the region where the energy was deposited had a sharp boundary (see Sect. 4.3.1) generating an extremely large jump (in energy) that made the code crash after several ten milliseconds. This initial jump is ten times smaller for the models with an energy deposition rate of 10^{50} erg/s. Therefore, the effect of the artificial deposition had not caused numerical problems in those cases. For model e51c090, the situation was not as critical as for model e51c100. The former one has been computed with a two times smaller angular resolution, and its increased numerical diffusion obviously helped to avoid the problem. However, in order to get model e51c100 to run, we had to include a time dependent deposition rate of the form:

$$\dot{E} = \begin{cases} 10^{51}\exp(-\frac{(t-t_0)}{t_0}) & \text{for } t < t_0; \\ 10^{51} & \text{for } t \geq t_0. \end{cases} \tag{4.18}$$

where $t_0 = 200\,\mathrm{ms}$. Hence, the deposition of energy proceeds in two stages: (1) exponential growth from $10^{51}/e$ erg/s to 10^{51} erg/s up to 200 ms, and (2) constant rate of 10^{51} erg/s afterwards. In addition, the edge of the deposition region was linearly smoothed over 3 cells in radial and angular direction (to decrease the jump between adjacent zones).

Model e51c090

The jet propagates faster than in any model with a deposition rate of 10^{50} erg/s. The time needed to reach the star surface is about 1.68 s (to be compared to 3.35 s for the previous models). $W_{\max} = 20.686$, which is almost equal to the value obtained for model e50c180 (but almost twice the value found for model e50c090, which has the same resolution). As before, $W_{\max}$ is located behind the largest (in size) recollimation shock. This shock is similar to the one in the previous models (Sect. 4.3.4). The half opening angle (in front of the shock) is $\sim 10°$, a bit larger than before, but the recollimation in the strongest shock is larger too. Behind the shock the half opening angle is $\sim 16°$, which then decreases about $6°$. The maximum specific internal energy is 3×10^{28} erg/g, which is about the same as in model e50c180. The central spine of high specific energy connecting blobs with high energy is also present. The baryon load is more than twice as large as that of models with a smaller deposition rate (see Table 4.1). A plausible explanation is that as the deposition rate is ten times larger much more material from the torus is pushed into the jet and, therefore, as this matter is very dense, the ejected mass is higher.

Model e51c100

With this better resolution we get larger Lorentz factors than those obtained with a deposition rate of 10^{50}erg/s. The maximum Lorentz factor is highly time dependent, and there are transients in which it can reach a value of 40, although after 1.2 s some kind of monotonic evolution is obtained, and the Lorentz factor increases non–uniformly from 22 to 33.3 (Fig. 4.12). The morphology is reacher than in the worst resolved model e51c090. It propagates faster than the corresponding 10^{50}erg/s model (see Fig. 4.9), but it is slower than model e51c090, because the time to reach the surface is 2.27 s. As mentioned in the previous section, this is a problem of resolution which was detected in the simulations of extragalactic jets too. In the present case, the lack of resolution near the axis has induced a ballistic propagation of model e51c090, which leads to a very high speed of the head ($0.6c$), preventing very high Lorentz factors within the beam (most of the material impinges against the terminal shock producing an efficient head propagation). The opening angle ($\sim 10°$) almost duplicates that of model e50c100 and it is much wider, roughly a factor of two, than the former (compare, *e.g.,* Fig. 4.7g with Fig. 4.12h), *i.e.,* the jet is less collimated.

The strong recollimation shock present in model e50c100 is not so evident here. Instead, several biconical shocks are observed within a very knotty beam. In addition, the Lorentz factor near the head of the jet is higher and, in the last model (Fig. 4.12h), a beam Lorentz factor as higher as 22 is reached very near the head. The high values of the Lorentz factor are produced by the fact that with this deposition rate, the central funnel is evacuated faster, and the mean density within the jet is about a factor 5 smaller than in model e50c100 (Fig. 4.13). Moreover, the largest deposition rate explains why, around the axial innermost region (near the limit of the deposition area), the density is as small as $3.5 \times 10^{-13}\,\mathrm{gr/cm^3}$, because the system has no time to feed the funnel with material coming from the lateral boundaries of the jet.

Models e51c090 and e51c100 have baryon loads (Table 4.1) that are twice larger

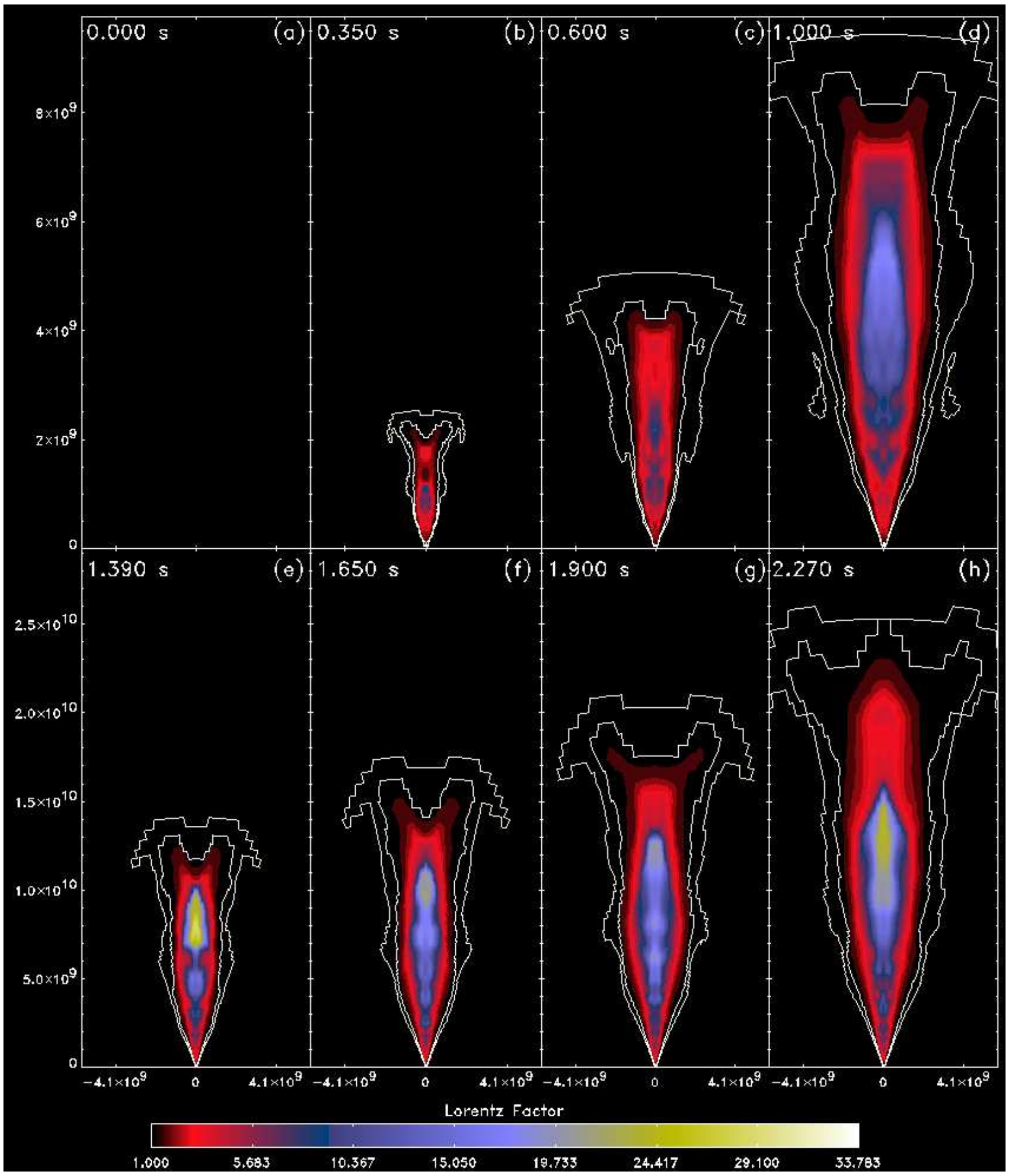

Fig. 4.12.— Same as Fig. 4.2, but for model e51c100 and showing the distribution of the Lorentz factor.

than in models with a 10^{50} erg/s deposition rate. This is due to the fact that models with a deposition rate of 10^{51} erg/s develop an extended cocoon of mildly relativistic velocities (see the extension of such layer comparing the white contours in Figs. 4.2 and 4.13) and relatively high mean density ($\sim 1\,\mathrm{g/cm^3}$), which increases consider-

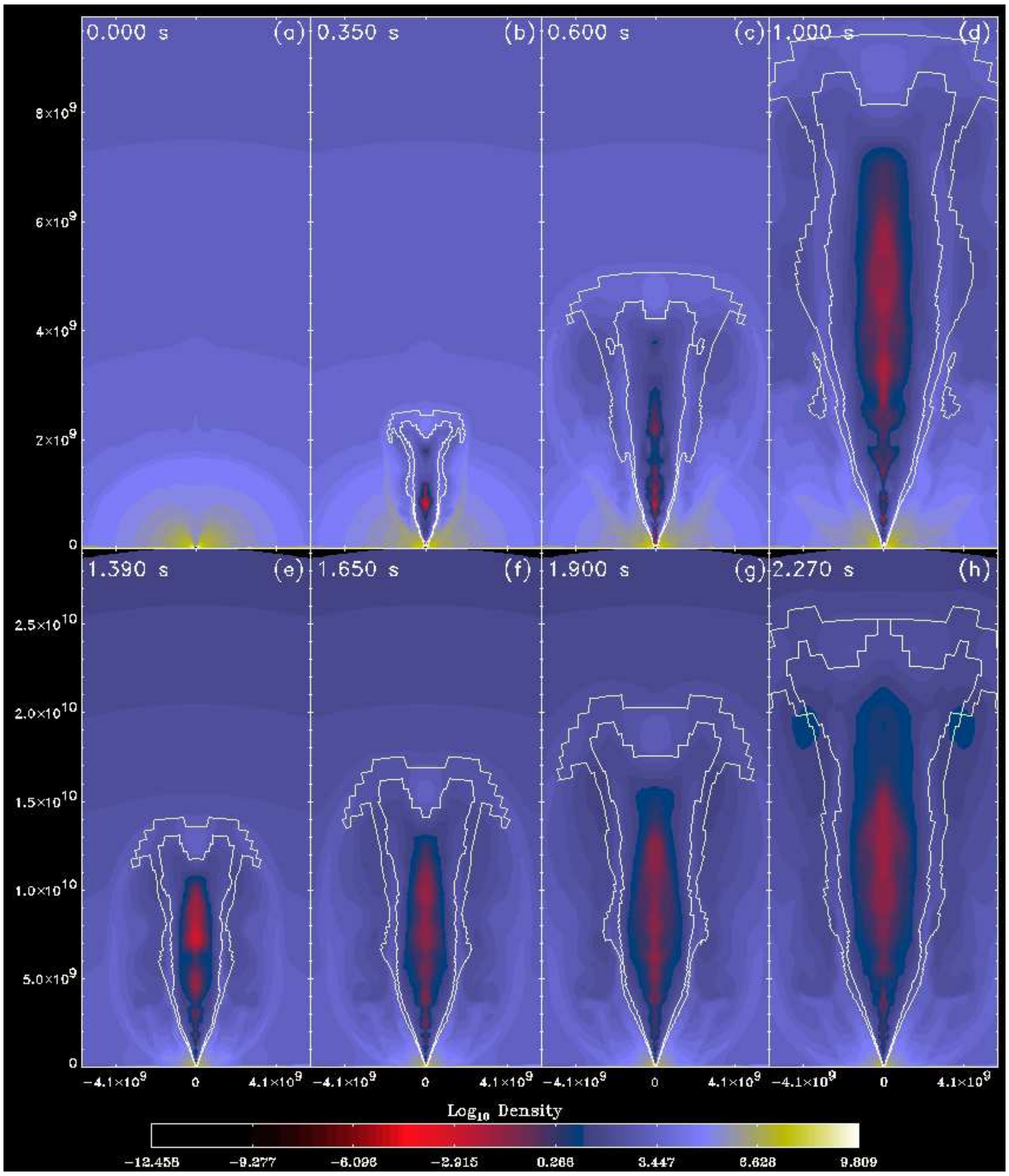

Fig. 4.13.— Same as Fig. 4.12, but showing the distribution of the rest–mass density.

ably the jet mass. However, looking at the whole evolution of the model e51c100 (including the post-breakout), the mass entrained into the jet increases slower with time than the energy released (similarly to model e50c100; see Sect. 4.3.4), so that η^{-1} decreases by a factor of two in less than 1.8 s.

In Fig. 4.10, the mass that crosses the innermost boundary as a function of time for different adjacent angular regions is presented for model e51c100. Comparing with the same figure for model e50c100 (left panel), one can notice that the behavior is similar, *i.e.*, , the total accreted mass is roughly the same. However, the largest energy deposition affects to the time at which the largest change of the slope of the curves happens: for model e50c100 it is $\sim 1.2\,\mathrm{ms}$, while for e51c100 is $\sim 1\,\mathrm{ms}$. Moreover, due to the fact that for e51c100 the deposition rate is not constant (and larger than that of model e50c100) at the beginning the slope of the curves is steeper. Additionally, the behavior of the curves up to $\sim 45°$, from 0.1 s to the end, is different in both models (steeper in e51c100). Another remarkable feature is that the the equatorial region contribute approximately the same to the total mass accreted because they are farther from the deposition volume (*i.e.*, it is less influenced by the details of the energy deposition).

4.3.6. Rapidly varying energy deposition rate

The model e50v100 includes a random varying energy deposition rate with average equal to 10^{50}erg/s. It has been produced in order to check if temporal variations make any significant difference for focusing, propagation or internal jet structure with respect to models with the same deposition rate but constant. Let us remain that the process of energy deposition by the neutrinos is dynamically variable because the region that produces them (the innermost part of the torus), may change with dynamical times of the order of several milliseconds. Consistently, we have imposed a varying energy deposition rate with the same time-variability (of the order of some milliseconds) and energy-variability (the energy deposition rate may change by more than one order of magnitude around the average rate) than that of a collapsar scenario (see MW99). Hence, the varying deposition rate mimics much better the phenomenon that is expected to happen in nature. Concerning the time variation of the deposition rate, we have to consider that 1 ms corresponds to a typical size of $1\,\mathrm{ms}\times c = 3\times 10^7\,\mathrm{cm}$. Nevertheless, our smaller cells (near the inner boundary) have sizes larger than $2\times 10^7\,\mathrm{cm}$, what means that we cannot capture properly the smallest time variations. However, as we are not interested right now in producing a realistic spectrum, and we are imposing a random pattern energy deposition (instead of being the result of a calculation involving energy transport and detailed microphysics), such detail is not relevant for the conclusions of the present work.

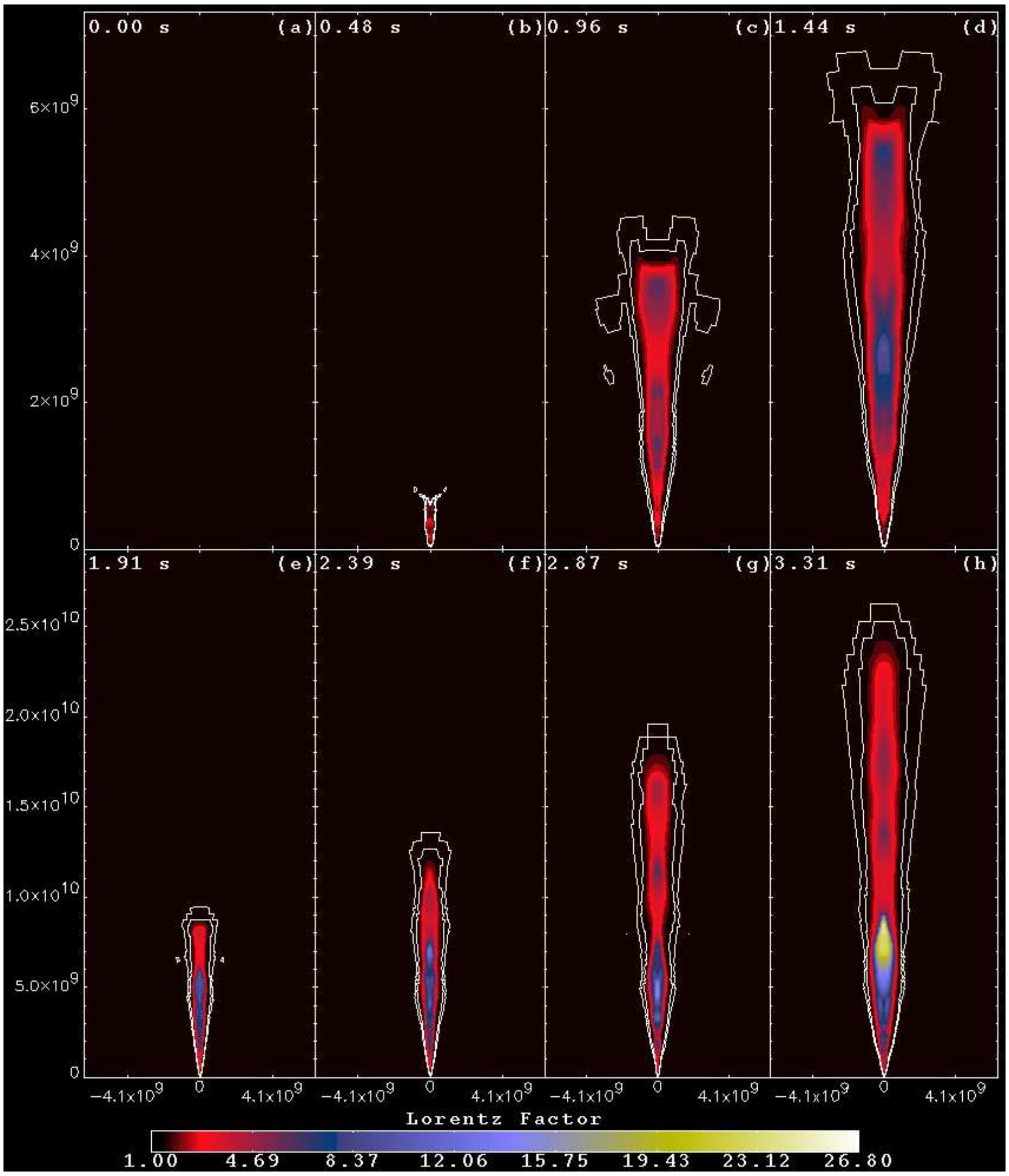

Fig. 4.14.— Same as Fig. 4.2 but for model e50v100 and showing the Lorentz factor distribution.

Fig. 4.14 shows the Lorentz factor evolution for this model. Compared with model e50c100 (Fig. 4.5), the structure is more knotty and rich in shocks, particularly in the firsts 10^9cm. Behind the largest recollimation shock (which is also present at roughly the same distance as in model e50c100) a noticeable blob-like structure is evident. Another remarkable difference is the maximum Lorentz factor reached, which is *almost twice* than the previous model ($W_{\max} = 26.81$), in spite of the fact that the energy deposited is, in average, the same. This means that a variable deposition rate is more efficient to convert internal energy into kinetic energy. We explain the highest efficiency in terms of the internal shocks, which are stronger and more numerous in model e50v100. As an example of this line of reasoning, let us consider the panels (f), (g) and (h) of Figs. 4.5 and 4.14. In Fig. 4.5g, at a distance $\sim 10^9$cm, a biconical shock is present (which is not in the previous panel, but has been generated between these two epochs). This shock is stronger in Fig. 4.14g, and when it collides with the precedent shock (the second shock is faster because it is moving into a channel of minor density than the medium that the first shock finds in its way) and evolves up to $\sim 7 \times 10^9$cm, accelerates much more the fluid than in the model e50c100 (the resulting Lorentz factor is more than twice).

The mean propagation speed is very similar in both cases (both models reach the surface in ~ 3.3s), although the instantaneous velocity of the jet's head is clearly different (comparing panel to panel in Figs. 4.5 and 4.14, the head is not at the same position, and the differences are even larger in other intermediate evolutionary states). Logically, this happens because the energy input varies in one case and not in the other, but since the mean deposition rate is the same, the mean velocity of the head is the same too. Moreover, the logarithmic grid in radial direction produces a decrement in resolution that tends to average the variations of model e50v100 and, therefore, this numerical effect makes more similar the latest stages of the evolution of both models.

The jet width is usually a bit larger in e50v100 than in e50c100 and the opening angle behind the largest recollimation shock is pretty small in both cases, although in Fig. 4.14h the model e50v100 seems to refocus after 1.7×10^{10}cm. However, this could be a transient effect.

4.3.7. Evolution after shock breakout

After reaching the star's surface, the relativistic jet should continue its propagation through a decreasing atmosphere. The situation then is such that an almost continuous release of energy (that of the jet) is put into a medium whose pressure is negligible compared with the one into the jet cavity, and whose density is of the same order (although as the jet will eventually move outwards in the ISM, density will decrease). This picture corresponds roughly to the propagation of a strong shock wave resulting from a strong explosion, that is, the instantaneous release of a large amount of energy in a relatively small volume. This problem has been studied, analytically by many authors, both in the Newtonian case (*e.g.,* Sedov 1959; Zel'dovich & Raizer 1966) and in the relativistic case (*e.g.,* Colgate & Johnson 1960; Johnson & McKee 1971; Elgroth 1971, 1972; Vitello & Salvati 1976; Blandford & McKee 1976; Shapiro 1979, 1980; Königl 1980). The main results of such works are: (i) the propagation of a planar explosion through a uniform medium follows a self-similar solution both in the classical (Zel'dovich & Raizer 1966) and in the relativistic case (Vitello & Salvati 1976), (ii) it leads to an increasing Lorentz factor with time, and (iii) a rapid decreasing of the post-shock density.

The finite light speed in RHD introduces a characteristic length scale, ct, into all initial value problems which, unlike the Newtonian case, precludes –in general– self-similar solutions. Colgate & Johnson (1960) calculated the relativistic Riemann invariants for the ultrarelativistic limit of a radiation dominated EOS, allowing to Johnson & McKee (1971) to obtain the solution of a planar, strong, ultrarelativistic shock into a cold gas of decreasing density. The method of characteristics used in the one-dimensional planar case could not be directly applied to spherical or cylindrical shocks. In these cases, only approximate solutions for strong, ultrarelativistic (spherical or cylindrical) expanding shocks were found by Elgroth (1972) assuming density gradients proportional to the radius. Blandford & McKee (1976) found an approximate similarity variable for the problem of spherically symmetric relativistic shocks (generated by a point explosion, or by a power supply varying as a power of time) moving into a uniform or decreasing atmosphere, which enabled them to find approximate similarity solutions (accurate to the lowest order in W^{-2}) and to conclude that the scale height of the shocked fluid in the extreme relativistic limit is of the of the order of R_s/W_s^2, where R_s is the radius of the shock and W_s its Lorentz factor.

The external density gradient determines whether the shock will accelerate or decelerate with time, both in the case of adiabatic shocks (Shapiro 1979) or radiative ones (Shapiro 1980). According to Shapiro (1979), the spherically symmetric solutions for relativistic shocks are inherently non-accelerating. The fact that they are self-similar solutions precludes the treatment of density profiles steep enough to produce shock acceleration. Only power laws $\rho \sim r^{-k}$, $k < 3$, are allowed, while the numerical two-dimensional simulations of Shapiro (1979), established that adiabatic point explosion requires $k > 3$. However, power laws as steep as $k > 3$ are unphysical, since they imply an infinite mass enclosed by the shock[13]. Actually, any physically meaningful density profile which is steep enough to accelerate the shock must contain a characteristic radius within which the profile is less steep than r^{-3}. Consistently, at early times, and up to such characteristic radius, the accelerating shock must be a decelerating shock, which prevents self-similar solutions.

The practical conclusion that we can extract for the collapsar model that we are proving is that the structure of the external medium surrounding the central engine will finally determinate the characteristics of the GRB shape (and those of the subsequent afterglow). As no exact analytic solution has been found in the arbitrary relativistic two-dimensional case, numerical simulations are crucial to clarify the outcome of the *proto-GRB*[14] after the breakout.

Along the previous sections we have analyzed the possibility of formation of a GRB in a collapsar model. The values of the Lorentz factor at the end of the simulation are still far from the ones requested in the fireball model (Sect. 4.1.1). However, according to PI99, internal shocks would be efficient at $R_{int} \sim 10^{13}$cm, because if the shocks arise earlier the radiation does not escape (the fireball is op-

---

[13]If $k > 3$, $M \propto \int_{R_0}^{R} r^{-k} dV \propto 1/(3-k)(R^{3-k} - R_0^{3-k})$, and when $R_0 \to 0 \Rightarrow M \to \infty$.

[14]We call proto-GRB to our relativistic jet because, actually, the Lorentz factor of the relativistic jet is between a factor of 3 to 5 bellow the assumed theoretical values, the baryon load is still larger than the expected in a GRB, etc. In addition, we are considering the formation phase in which the *proto-fireball* is still optically thick, hence, we cannot observe directly such stage of evolution but a later one (if, at the end, the proto-GRB becomes a GRB).

tically thick). In our case, the relativistic jet has reached at most 3×10^{10} cm, 100 times smaller than the distance for the system to be optically thin. This means that if we want to produce a real GRB, a longer evolution should be considered. With this aim, we have extended our computations to a larger domain including an atmosphere for the Wolf-Rayet star.

In order to satisfy the conditions to get an accelerating shock, we have generated a Gaussian atmosphere matching an external uniform medium of the form:

$$\rho(r) = \begin{cases} \rho(R)\exp[-b(r - R_a)^2] & \text{with } b = -\ln\left(\dfrac{\rho(R)}{\rho_e}\right) \text{ for } R < r < R_a; \\ \rho_e & \text{for } R_a < r < R_t. \end{cases} \tag{4.19}$$

ρ_e is the value of the external density outside the atmosphere. The atmosphere extends from $r = R$ (the star's surface) to $r = R_a$. For the pressure, the same profile is used to join the star's surface ($p = p(R)\,\mathrm{dyn/cm^2}$) with the ISM ($p = 10^{-8}p(R)\,\mathrm{dyn/cm^2}$). The rest of thermodynamical variables are got from the EOS. The velocities outside the star have been taken to match that of the surface and decaying radially with $r^{1/2}$, so they are very close to zero in the whole external domain.

The values of the parameters of the atmosphere are: $R_a = 1.8R$, $R_t = 2.54R$, $\rho_e = 10^{-5}\mathrm{g/cm^3}$. Such a election of $p(R)$ and ρ_e is somewhat arbitrary and, therefore, it does not emulate exactly the expected values for the medium surrounding a Wolf-Rayet star (which most probably show a decay of the thermodynamical variables as r^{-2}). However, with a structure like this we can explore the effects of the proto-GRB propagation on a uniform and non-uniform medium. Additionally, the Gaussian profile of the innermost part of the atmosphere is steepest than any radial power-law gradient, thus, satisfying qualitatively the requests of Shapiro (1979) concerning the ambient stratification (see above), in order to produce relativistic expanding shocks that accelerate.

The evolution after the surface breakout has been followed for the models e50c100 and e51c100 (however, the analysis of e51c100 is still under progress, and is not going to be presented here). The numerical domain has been extended with 70 additional radial cells. A picture of the whole evolution (after the jet breakout) is shown in Fig. 4.15. The time needed for the jet to reach R_t, from the star's surface, is $\sim 1.8s$. Hence, the mean propagation velocity of the frontal bow shock in this pe-

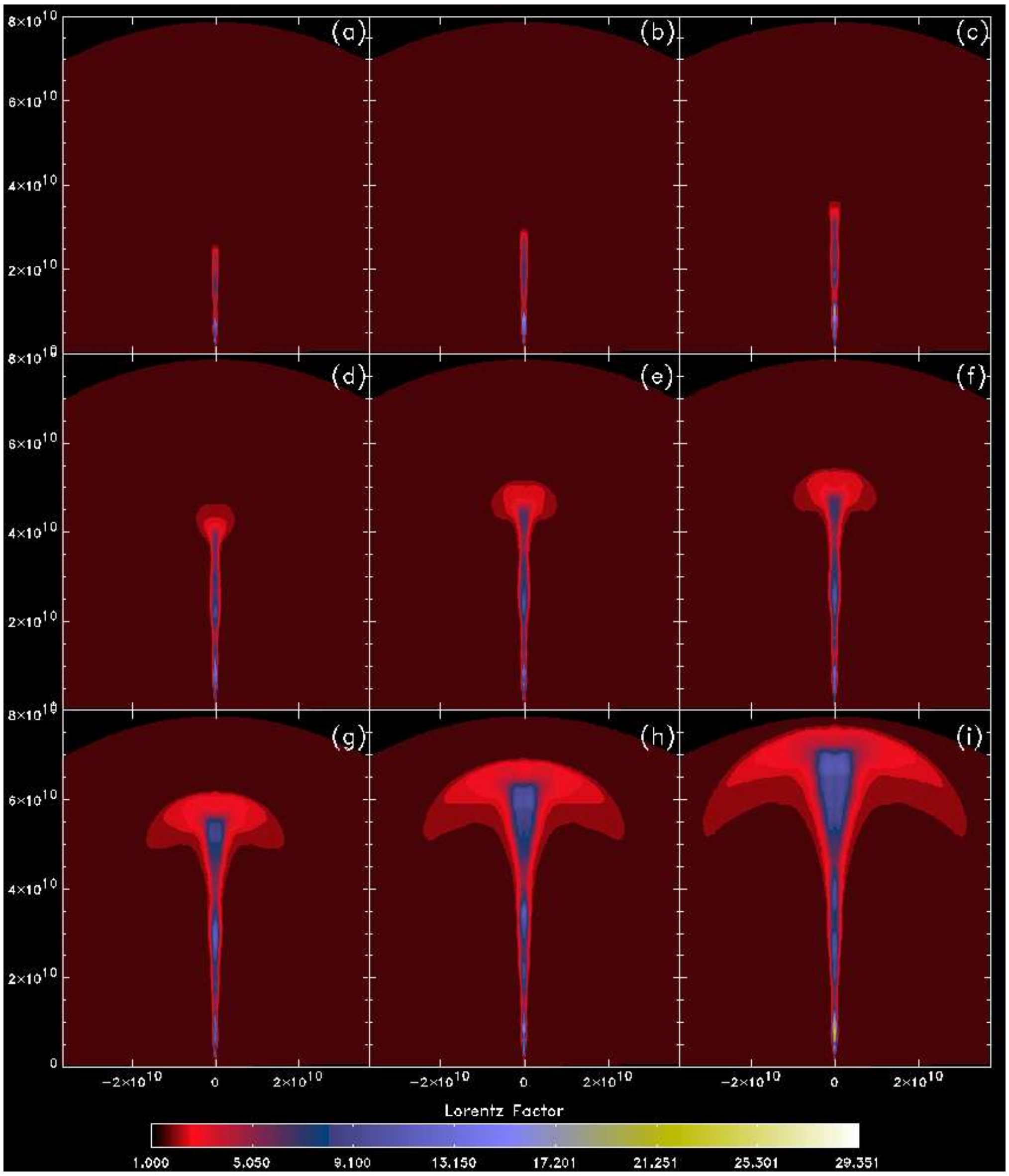

Fig. 4.15.— Nine colored-contour maps of the Lorentz Factor at different evolution times for the model e50c100 after the breakout. X and Y axis measure distance in centimeters. From top to bottom and left to right the corresponding snapshot times are: 3.39, 3.65, 3.91, 4.17, 4.34, 4.43, 4.69, 4.95 and 5.21 s.

riod is $\sim 0.85c$, which is almost three times faster than the velocity of the head into the star ($0.3c$). Furthermore, after the breakout it is possible to distinguish several epochs characterized by different axial propagation speeds and sideways expansion velocities[15]:

1. The first phase lasts 0.25 s during which both, the lateral expansion and the axial distance grow proportionally to $t^{1.6}$ (lateral expansion) and $t^{1.7}$ (axial distance) (see Fig. 4.16). This epoch is dominated by the inertia of the jet (that remains highly collimated) coming from the star interior Fig. 4.15a). The head's velocity during this phase is $0.48c$. The *ram pressure* near the terminal contact discontinuity ($\bar{F}_{\rm S}$)[16] increases as $\sim t^{0.7}$, while the mean pressure grows as $\sim t^{0.4}$. Moreover $\bar{F}_{\rm S}$ is larger than the mean pressure, which supports the jet-shaped expansion.

2. The second phase (of ~ 0.56 s) is characterized by a large acceleration of the head of the jet up to a velocity of $0.91c$. The reason of such acceleration is the steepest external density gradient along with the $\bar{F}_{\rm S}$ dominance (over the pressure). The sideways expansion is subrelativistic (the expansion velocity being $\sim 0.19c$) and during this stage it grows slower than in the previous phase ($\sim t^{1.0}$). The opening angle increases up to roughly $10°$. In this stage the sideways growth is due to the finite radius of the jet which penetrates the atmosphere (not to a lateral expansion of the beam).

3. The last part of the evolution is marked by the moment in which the bow-shock reaches the homogeneous part of the atmosphere. Here the resistance to the axial advance does not decrease any more while it still does it sideways, leading to a rapid lateral spreading. In fact, one can notice from Fig. 4.16 that

[15]The sideways expansion velocity is calculated as the maximum of the lateral displacements of the pressure bubble for each time. Hence, such velocity does not correspond to a physical point because, for different times, the maximal expansion can take place at different points.

[16]The precise definition of this quantity is $\bar{F}_{\rm S} = (\int_M S_z v_z dV)/(\int_M dV)$, where M is a volume around the terminal contact discontinuity. The quantity is an indicator of how important is the axial momentum, in the morphology of the bubble, compared with the mean pressure within the bubble. If this flux is larger than the mean pressure a "cylindrical" or "jet-shaped" morphology is expected. If pressure dominates the bubble expansion will be spherical.

the axial growth rate slightly decreases (now it only increases as $t^{1.3}$). The lateral expansion rate changes drastically (see the slope change in dashed line of Fig. 4.16), and the velocity of expansion arrives to be $(1.4 \pm 0.42)c$, *i.e.*, , it grows faster than the axial expansion (solid line). The error that we have assigned to this measure comes from the uncertainty in the determination of the position of the bubble boundary associated to the numerical diffusion of the algorithm (that may spread over 2 or 3 cells the bubble–to–external medium blast wave) and the fact that the radial mesh is logarithmic and some of the external cells may have a relatively large size (the maximum mesh spacing is 1.07×10^9 cm). This behavior in the lateral direction is due to the external density gradient, because the point of maximal expansion coincides with the uniform/non-uniform atmosphere interphase, which means that the material expanding sideways is still sensitive the density gradient, while the axial part of the jet is propagating through a uniform medium. The expansion velocity in the last stage tends rapidly to become relativistic, although in most of the evolution it is subrelativistic or mildly relativistic. This effect produces a more symmetric expansion, tending to be spherical instead of jet-like. Furthermore, both the mean pressure and $\bar{F}_{\rm S}$ decay very fast with time as $\sim t^{-4.8}$ and $\sim t^{4.0}$, respectively.

The evolution of the maximum value of the Lorentz factor is similar to that in the pre-breakout epoch. As before, it is reached behind the first large recollimation shock, which in its turn moves from $\sim 10^{10}$ cm (Fig. 4.15a) to $\sim 1.5 \times 10^{10}$ cm (Fig. 4.15i) during the post-breakout evolution. At the end of the simulation, the maximum Lorentz factor is 29.35, and the beam material just behind the terminal contact discontinuity (between the head and the external medium) has increased its mean Lorentz factor from ~ 4 (at the breakout) to ~ 9. This values are consistent with an adiabatic expansion because we have checked that along the axis (which is actually a fluid line) the product hW is constant and approximately equal to 15. Around the head the fluid moves mainly along the axis (Fig. 4.17), and near the lateral boundaries of the expanding bubble a strong velocity in the θ direction appears soon after the breakout. The Lorentz factor near the boundaries of the jet cavity grows from ~ 1 (at the beginning of the breakout) to $\sim 2.5 - 5$ (values in the maximal expansion region and in the axis, respectively).

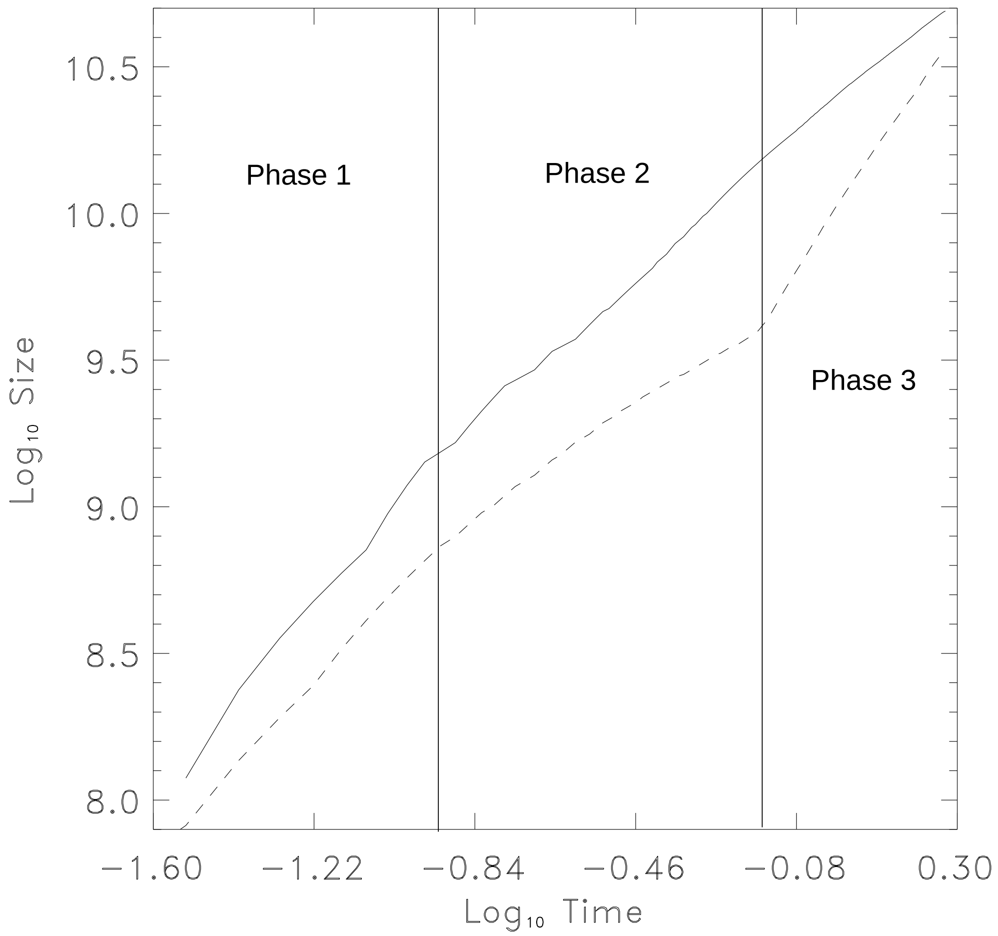

Fig. 4.16.— Evolution of the axial (solid line) and lateral (dashed line) expansions after the jet break out. The axial expansion is calculated detecting the head of the jet and subtracting from it the radius of the star (the breakout point). The lateral expansion is calculated according to footnote 15. Additionally, note that from the sideways expansion distance we subtract the initial radius of the beam.

The shape of the expanding bubble is longer than wider (see Fig. 4.18) during the whole post-breakout evolution and, therefore, we can continue referring to it as a "jet" (see Sect. 4.1.4). However, when the jet reaches the uniform part of the atmosphere, as the sideways expansion is faster, the shape is appreciably widen. We have not followed the evolution long enough to see what happens when most of the bubble propagates outside the declining atmosphere. Nevertheless, we can

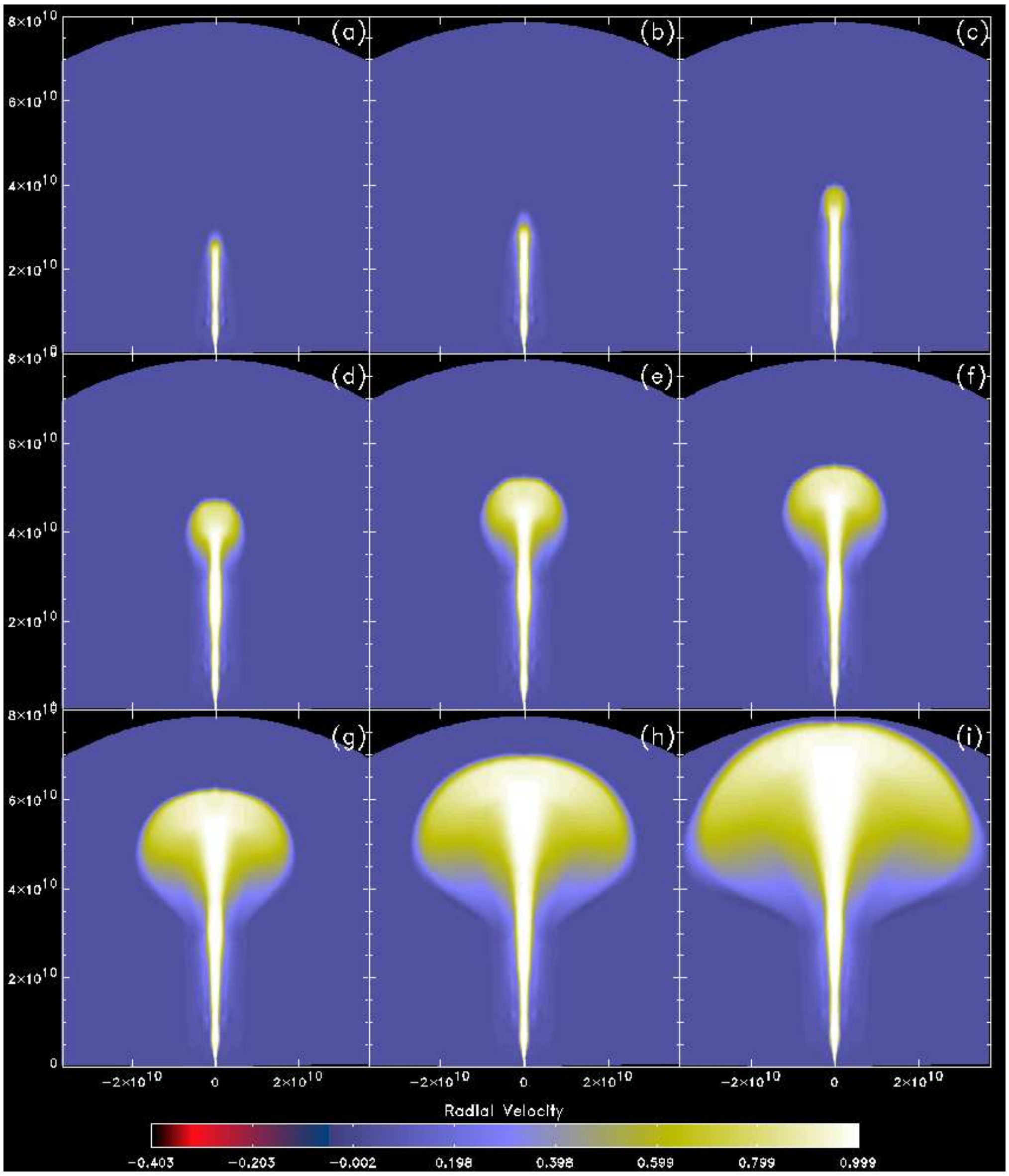

Fig. 4.17.— Same as Fig. 4.15 but for the radial velocity.

infer from Fig. 4.16 that the trend is to decrease the widening rate in a way similar to what has happened with the axial expansion. The reason is that being most of the bubble inside an homogeneous medium, and considering that at larger distances the bubble will be pressure driven (which would be particularly true if the energy deposition is switched-off), it should tend to expand isotropically.

Over and above all these considerations, it remains true that the evolution has been followed only up to a distance 100 times smaller than R_{int}, and our results are still far to establish whether we can produce a "real" GRB or not. Anyway, the total energy deposited near the inner boundary, is only 5.2×10^{50} erg, and the total evolution time is 5.2 s. Both values are in agreement with the energetics and duration of a generic cosmological GRB (see Sect. 4.1).

Another important remark is that our expansion corresponds to a mildly relativistic bow-shock propagation. However, the fireball model (Sect. 4.1.1) assumes an ultrarelativistic expansion to overcome the compactness problem. Such a problem stems from the assumption that the size of the sources emitting the observed radiation is determined by the observed variability time scale. In addition, the non-thermal spectra of GRBs indicate with certainty that the sources must be optically thin. This has been taken as an indication of the fact that the emission of the GRBs comes from very large distances (compared with the bursters). Thus our breakout simulation corresponds to a previous stage of the GRB evolution: the formation and acceleration of the fireball. Obviously, in order to reach the ultrarelativistic regime, first the plasma has to be accelerated, and in the initial part of the evolution, the propagation must include a subrelativistic to mildly relativistic regime. Such regime can not be studied analytically and, hence, the numerical simulations become necessary. Our results show that the pre-breakout relativistic jet evolves getting a mildly relativistic propagation speed (the head moves in the final stages at $0.91c$), and it seems that the trend is to accelerate. Additionally, the lateral spreading is present and the expansion velocity tends to the light speed, in agreement with the estimate of Sari, Piran & Halpern (1999), and being less consistent with the estimate of Rhoads (1999) (who assumes a lateral spreading velocity of $c_s = c/\sqrt{3}$ in the comoving fluid frame).

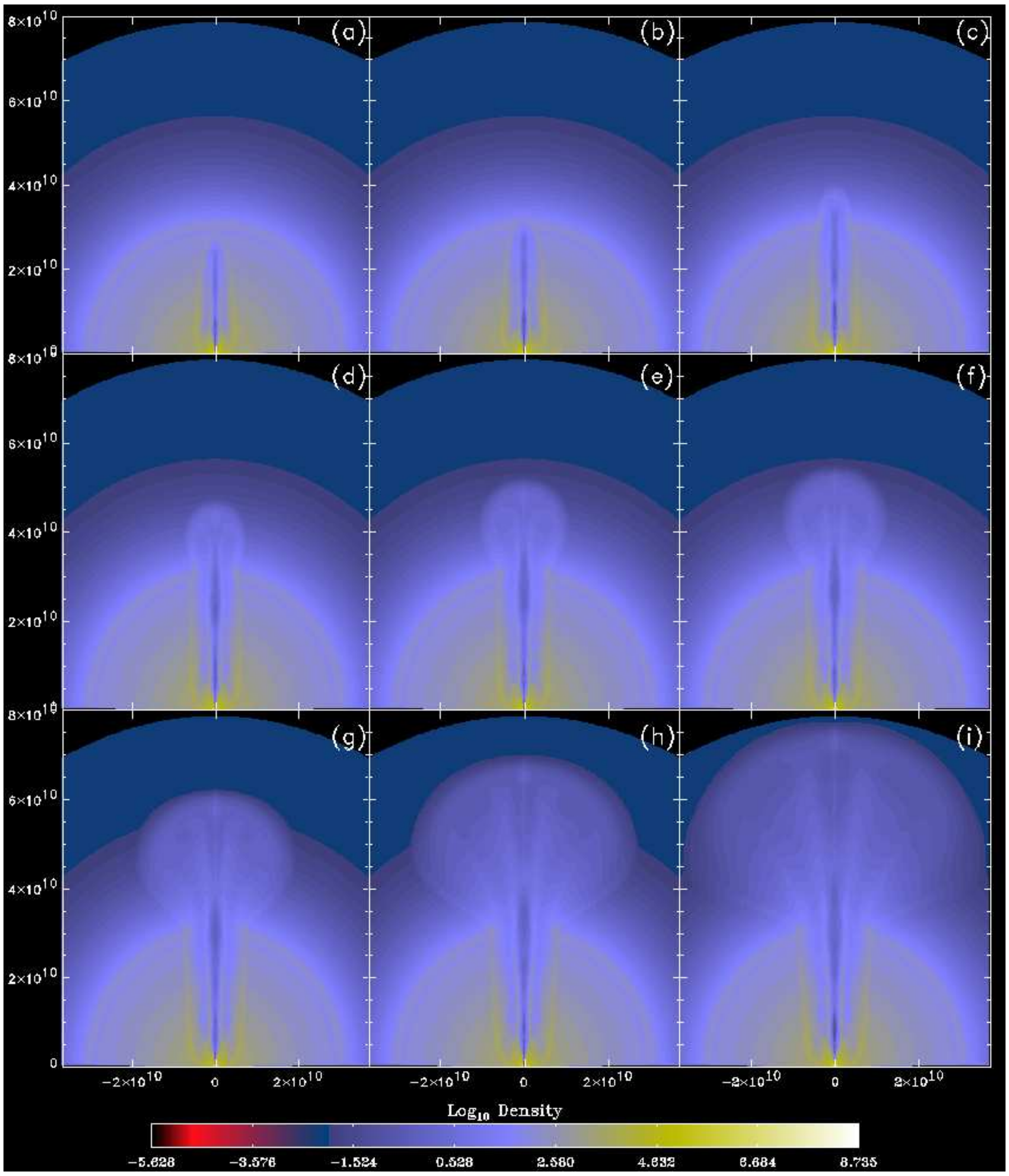

Fig. 4.18.— Same as Fig. 4.15 but for the logarithm of the rest–mass density.

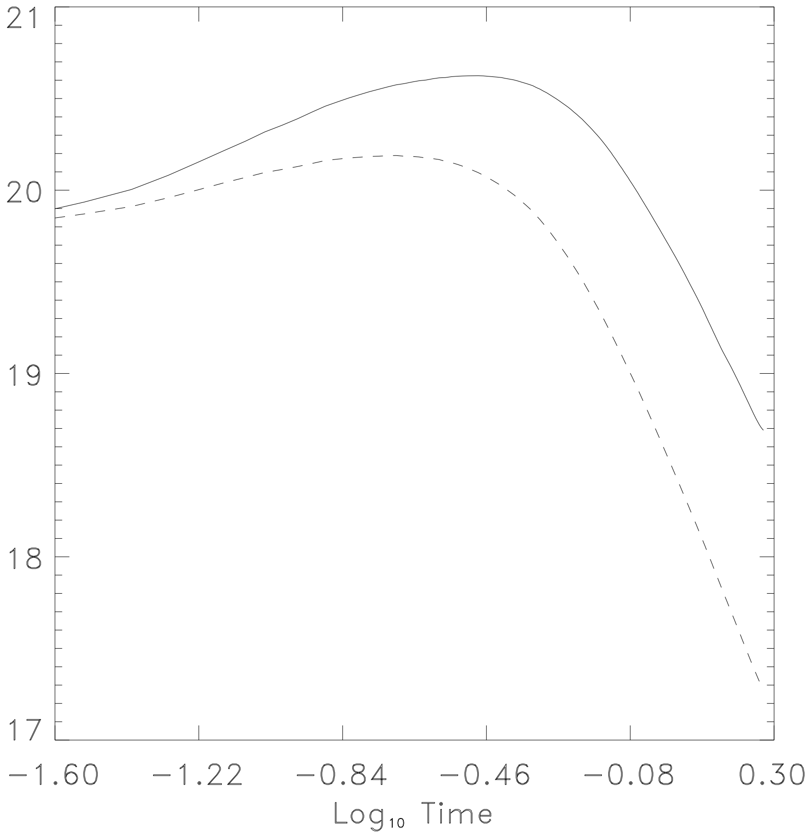

Fig. 4.19.— Evolution of the mean pressure into the jet cavity after the jet breakout (dashed line) and mean axial momentum flux in the neighborhood of the jet's head (solid line) *versus* time.

4.4. Conclusions and outlook

Using a collapsar progenitor model of MW99 we have simulated the process of energy deposition that may happen in a realistic Wolf-Rayet star. The result of the deposition has been the formation and propagation of an axisymmetric jet through the mantle and envelope of a collapsing massive star. We have studied two deposition rates (10^{50} and 10^{51} erg/s) which bracket the current estimates for the GRBs energies assuming a cosmological distance. Highly relativistic and collimated outflows have been found. The maximum (final) Lorentz factor reached has happened in the model e51c100 ($W_{\rm max}$ = 33), and it has occurred at the end of the pre-breakout phase (*i.e.,* just before the jet reaches the surface of the star).[17] For the largest energy deposition rate, the jet and in particular the cocoon are less collimated, because when the jet is driven harder it also expands stronger laterally.

The rest-mass density and the internal energy show strong spatial and temporal variations within the jet giving rise to a very inhomogeneous baryon loading. The average baryon load of the jet is $\bar{\eta}^{-1} \sim 1$, but some parts of the jet have a baryon load $\sim 10^{-5}$ or even less. After jet breakout $\bar{\eta}^{-1}$ decreases by a factor of four in less than 1.8 s. If this trend continues $\bar{\eta}^{-1} \sim 10^{-3}$ is reached in less than 9 s.

We have studied the influence of the grid resolution on the results and we have seen that very poor resolutions can underestimate the values of the Lorentz factor and overestimate the mean density inside the jet and the head's velocity. We can conclude that, at least an angular zoning of $0.5°$ around the axis and covering 3 beam radii is the minimum resolution to obtain a convergent result.

The results of a varying energy deposition (which emulates more accurately the real process) indicate that the formation of a large number of internal shocks helps in the beam fluid acceleration. As the mean energy released in models e50c100 and e50v100 is the same, the mean head speed is roughly the same although the beam maximum Lorentz factor is higher (by a factor of two) in the non constant case.

The evolution after the jet breakout is clearly influenced by thermodynamical gradients in the external medium and the final value of the external density ρ_e. Using an atmosphere with a Gaussian profile near the star surface and a constant value afterwards, we have found several evolutionary stages. The different phases are correlated with the times at which the jet reaches the points of change of gradient in the atmosphere and the relative importance of the axial momentum flux compared with the mean pressure in the material surrounded by the bow shock. Anyway, considering the whole evolution, the maximum Lorentz factor grows up to almost 30 in some parts of the beam, and the external shock expands sideways faster than he head advances. However, for this particular election of atmosphere (and ρ_e) the propagation of the bow shock is only mildly relativistic and the main characteristics

[17] During the post-breakout phase of e51c100 (not shown here) the maximum Lorentz factor in the final model is ~ 46, with some transients in which $W_{\max} \sim 50$.

of our simulations cannot still account for the observational properties of the GRBs or their afterglows.

From the preliminar analysis of the post-breakout evolution of the model e51c100 it comes out that at the end of the simulation, $\sim 2\,M_\odot$ have a Lorentz factor of less than three, $3\times10^{-4}\,M_\odot$ move with $3 \leq W < 10$, and for $2\,10^{-6}\,M_\odot$ the Lorentz factor $W \geq 10$ (the latter two masses reduce to $2\times10^{-5}\,M_\odot$ and $2\times10^{-7}\,M_\odot$ for model e50c100). Except for the very early evolution ($t < 1\,\mathrm{s}$) the amount of matter moving at moderate ($3 \leq W < 10$) and highly ($W \geq 10$) relativistic velocities increases by a factor ~ 3 every second, *i.e.,* when the central engine is active for another 5 s at the assumed energy deposition rate an amount of matter with mass $\sim 10^{-4}\,M_\odot$ will move with $W \geq 10$. As the maximum Lorentz factor is also rapidly increasing, it is not unlikely that maximal Lorentz factors of several hundreds can be reached before the central engine is shut off.

We may regard our set of numerical models as simulations of a proto-GRB, because the scales involved in the problem ($r \lesssim 8\times10^{11}$ cm) are still far by more than one order of magnitude from the typical distances at which the fireball becomes optically thin ($R_{int} \sim 10^{13}$ cm). Consistently, if a GRB would result from some of them, further material acceleration is required.

Concerning the future work, a prompt improvement of the method applied here would include the deposition of momentum along with energy, because, the real process of $\nu\bar{\nu}$–annihilation does not only release energy into the system but also momentum. Taking into account the particular configuration of the torus, this momentum will help in pushing the matter outwards and, hence, in getting larger Lorentz factors for the relativistic proto-fireball.

Another line of work may be to study the influence on the final ejecta of variations in the initial model. For example, following MW99 work, we can try to apply GENESIS to initial models containing an inner boundary closer to the even horizon of the BH. Releasing energy at shorter distances to the BH emulates better the energy deposition by neutrinos because the into the inner parts of the star the temperature is higher and, therefore, the neutrino fluxes are larger (*i.e.,* the number of neutrinos that could interact releasing energy is larger).

In the above mentioned direction we can consider different astrophysical scenarios like, *e.g.*, NS/NS mergers (similar study than that of Ruffert & Janka (1999a) could be done using a relativistic hydro-code like GENESIS) or, NS/BH mergers (like in Ruffert & Janka 1999b). However, such merging scenarios would require a more accurate treatment of the gravitational force. Actually, in order to be fully consistent, a dynamical space-time will be necessary to address properly if these scenarios are suitable to produce GRBs. We have future plans to use the null formulation of the Einstein equations to evolve the space-time metric in the NS/BH merger scenario that the Newtonian studies (Ruffert & Janka 1999b) have pointed out as the most favorable to be GRB progenitor.

More realistic EOS and an feasible transport scheme are necessary to improve the micro-physics. An improved EOS would provide to the code realistic values for the neutrinos' production and will handle more properly with the denser parts of the star (or the merger). In addition, the transport scheme will allow us to include the right energy deposition rate at every point of our domain.

The propagation of the jet into the circumstellar medium depends on its stratification. Thus, further simulations with different environments are planned. It would be interesting and more realistic to consider (outside of the star) stellar winds with a declining density falling as r^{-2}, because this environments are the ones expected around collapsars. We also want to examine progenitors of different size and different internal structure. Larger stars provide longer inertial confinement of the jet probably leading to larger Lorentz factors, if the central engine works at least until the jet reaches the stellar surface. Stars with a less pronounced or even no central torus will provide less initial collimation. As our simulations have not been pushed far enough in time yet, they can (at the present stage) neither account for the observational properties of GRBs nor their afterglows. Hence, we plan to extend them to later times and larger radii ($\sim 10^{13}\,\mathrm{cm}$) using adaptive mesh refinement (AMR) or multi-resolution techniques.